doi:10.26443/seismica.v4i2.1303

Seismicity and Surface Deformation in Kamanjab Inlier, Northern Namibia

Moses T. Angombe * [1,2,3,4], **Justin Chien** [1,2], **Guy Salomon** [5], **Yajing Liu** [2], **Christie D. Rowe** [2,6], **Mako Sitali** [3], **Shatimwene Shipena** [3]

[1]Co-first authorship, [2]Department of Earth and Planetary Sciences, McGill University, Montréal, Québec, Canada, [3]Department of Geological Survey of Namibia, Ministry of Mines and Energy, Windhoek, Namibia, [4]Now at: Department of Geology, Lakehead University, Thunder Bay, Ontario, Canada, [5]School of Earth and Ocean Sciences, University of Victoria, Victoria, British Columbia, Canada, [6]Now at: Nevada Seismological Laboratory, University of Nevada, Reno, Reno, Nevada, United States of America

Author contributions: *Conceptualization*: Moses T. Angombe. *Methodology*: Moses T. Angombe, Justin Chien, Guy Salomon. *Formal Analysis*: Moses T. Angombe, Justin Chien, Guy Salomon. *Investigation*: Moses T. Angombe, Justin Chien, Guy Salomon. *Resources*: Moses T. Angombe, Justin Chien, Guy Salomon, Mako Sitali, Shatimwene Shipena. *Writing - original draft*: Moses T. Angombe, Justin Chien, Guy Salomon. *Writing - Review & Editing*: Moses T. Angombe, Justin Chien, Guy Salomon, Christie Rowe, Yajing Liu. *Visualization*: Moses T. Angombe, Justin Chien, Guy Salomon. *Supervision*: Christie Rowe, Yajing Liu. *Project administration*: Moses T. Angombe. *Funding acquisition*: Moses T. Angombe, Christie Rowe, Yajing Liu.

Abstract The last two decades have seen the onset of felt earthquakes, including occasionally damaging events, in the Kamanjab Inlier, a block of Paleoproterozoic crystalline basement in northern Namibia. The Geological Survey of Namibia (GSN) and the Council for Geoscience, South Africa (CGS) deployed a temporary network of 10 seismic stations within the Kamanjab Inlier from June to September 2018 and cataloged ∼1500 events. We used a neural network-based earthquake phase detector, EQTransformer, to enhance the published GSN catalog to ≥9000 detections. The double-difference earthquake relocation of ∼4500 events reveals two distinct major and three minor spatial clusters that we interpret as local discrete faults that intersect the NE-dipping seismogenic fault of the 4 April 2021 M_w 5.4 earthquake, which is the largest instrumentally recorded earthquake in Namibia to date. We name the M_w 5.4 host fault "Anker Fault" and constrain its orientation using Sentinel 1 Interferometric Satellite Aperture Radar (InSAR) to image surface uplift and subsidence patterns. Given the sudden onset of the 2018 seismic activity and the absence of dams, mineral or energy exploration projects nearby, we eliminated the possibility of anthropogenic triggering. We suggest that the proximal cause for 2018 seismicity is shallow groundwater migration, possibly associated with nearby hot springs and modulated by tidal forces. The Kamanjab Inlier area has shown an increase in the number and magnitude of earthquakes from 2018 to 2021, which could pose a seismic hazard in the future. Our study introduces an earthquake detection and relocation workflow that can be adopted for regions with limited instrumentation.

Production Editor: Carmine Galasso
Handling Editor: Matt Ikari
Copy & Layout Editor: Sarah Jaye Oliva

Signed reviewer(s): Victoria Stevens

Received: March 14, 2024
Accepted: May 11, 2025
Published: July 14, 2025

Tsâlkhahe //oasa Nē ge !kharu /gamdisi (20) kurigu //aeb !nâ i /gui/guibe doe!kharu ra !hū≠ guwi !nôade Kamanjab ≠ganagab !na Namibiab /Apas !nâ gere hō!âhe, tsî !nākorobe ≠khôaba gere hā-ūde. Namibiab !Hū≠ans Ôa!nâs !Gae//ares (GSN), Council for Geoscience, South Africa (CGS) ge //aerob /gaiba nî sîsen //khā disi (10) seismik mâ!khaide tamas kai io berodi Gamalaeba xu Tara//khumu //khâb 2018 kōse ge mā≠ui tsî //gau≠uisenkai 1500 //axasiga !khō//nâs !aroma. ¬ Sida ge !hū≠guwib /nō//nâ-ūdadi hîa komputer-huib /khā Kurusa di (neural) !gae//aresens ai !gao!gaosa !hū≠guwi kōhō-ū !âga ra sisenū, EQTransformerdi, hîa ra GSN //gau≠uisa /gai/gai!nâdi >9000 kōhō-ūdadi tsî /asa !khaidi ai ≠nûisadi hîa 4500 //axasiga a !nâ !khō//nâ //khāti tsîna ≠nui≠ga hâ. Sida /gam!nâguse ra sîsen /asa !khai Kōhō-ūdas ge /gam dana tsî !nona ≠khari mûmûsa īsigu tsîna tamas kha io !kharaga !nâgu !ā≠uisab !khomde ge ≠hai≠hai hîa sâusase ra doe!kharu !hū≠guwi!âdi ase a //gui!âhe //khāde, NE seismoegnik tsū/-gaugu tamas kha io /gora- īsiroga ra //gauga, ai! âkam tsi /ae//aeb !nâ ge ī !hū≠guwigu !nâ /nō//nâdi hia ge 04 !Hoa≠khaib 2021 dis ai ge M_w 5.4. M_w 5.4 ge hoadi xa kai sîsenū xū!nôa Namibiab !nâ ge xoa//guihen hoan xa. //îsa da ge "Anker Fault" ti ge ≠gai tsî //îs di !uru≠âibasensa ge /oro/oro Sentinel 1 Interferometric Satellite Aperture Radar (InSAR) ra sîsenūse îda īsigu tsî !khō//nâhe ra /gauga mū!ā //khā. Nē !âubesenhe tama seismic //axasigu //-gats ga kō, tsî meneralna di /khais tamas ka io /gaib sîsen≠uisen/gaugu //ga da ge ī//khāsib anthropogenik diba ra //ara≠ui. Sida ra ao//guis ge //nā 2018 seismic doe!kharu ra !hū≠guwiga ge !aroma //axasi-/kai tama tsî a ≠heresa, !hūbaib !hūb!naka ra !khoe //gami di doebēs /kha i ge ī//khāsib ga hâ o a !gae//aresa /nî /audi /game ūhâdi /kha.

Omaoronganisiro Ape ozombura omirongo vi vari nda kapita nao pa kara omanyinganyingiro wehi peke peke nu mu nao mwa kara nga nyona orukondwa rwaNamibia komanene wehi moKamajab Inlier. Onganda ndji ongondononene yomawe novize vyomehi yaNamibia (Geological Survey of Namibia (GSN)) rwa ka twapo ozosasiona omurongo (10) ndu ze rekena omikato vyomanyinganyingiro wehi nda kara mbo okuza ku Ngarano nga ku Ndengani yo 2018. Nu za rekena omanyinganyingiro wehi 1500.

*Moses Angombe: moses.angombe@mail.mcgill.ca

Mo sasiona twa ungurisa otungovi tuma tu va tere okumuna kutja omanyinganyingiro wehi ye ripi. Kwa munika omanyinganyingiro >9000 okuza mu ingo 4500 ya tjiukwa kutja ya zapi. Otuveze pupa munika omanyinganyingiro ye raisa okutja tjinene omanyinganyingiro nga yeri movimbumba ovinene vi vari na vyarwe vi tatu mbi ri kehi ya nao. Omakondononeno inga ya raisa kutja mehi muna omuta mbu tupuka okuza komanene ngaa komamuho wehi. Inga ongeri omanyinganyingiro wehi omanenene nga tji u kisiwa moNamibia nu yari nomasa wo M_w 5.4. Omuta mbwi wa rukwa "Anker Fault" nu wa munikwa mo mepa yehi muya perendwa iyo satalite nu ena romepa ndji o Sentinel 1 Interferometric Satellite Aperture Radar (InSAR). Motjimbe tjo kuhina ozomine poo omapahero womawe poo ovize vyomehi poruveze ndwi mbya tja vi tjita okutja pe kare omanyinganyingiro wehi, twa muna okutja omanyinganyingiro inga ka ye eterwa i yovitjitwa vyovandu posya ovihomonena. Otja koumune wetu omanyinganyingiro wehi yo 2018 ka yari omakoto nu nga ka tjita omakaendjero womeva yokehi yehi. Omakaendjero womeva yokehi yehi ya hakaena kuna omeva omapyu nge ri kehi yehi (hot spring) mozondendera ndo.

Oontentekelihapu Okuza oomvula omilongo-mbali (20) dhakapita, okwa konekwa ha kuholoka omakuthikuthi gekakamo lyevi goodjele dha yooloka koshitopolwa shevi sho kuumbangalantu waNamibia, unene momudhingoloko gwevi gwaKamanjab. Omakakamo gevi ngano gamwe ohaga uvika omayinyengo gago na poompito dhimwme oga e ta nokuli omayonagulo momudhingoloko. Oshikadjo shuunongononi wevi moshilongo shedhina Geological Survey of Namibia (GSN) no and Council for Geoscience, South Africa (CGS) osha ningi omapekaapeko gomuule okutala shoka tashi etitha omakuthikuthi ngaka. GSN oya longitha nokudhika omashina gopaunongononi nogo pashinanena ge li omulongo (10) momudhingoloko moka hamu holoka omakakamo gevi, shaningwa pakathimbo okutameka mu-Juni sigo omuSeptemba 2018. Omashina oga li ga yakula omakakamo gevi ga adha lwopeyovi limwe nomathele gatano(1500) lwaampo . Okwa li woo kwa longithwa uungomba womuule (wedhina EQTransfomer) hayi longitha ocomputer djono nokuli ya mono omakakamo gevi ga gwedhwapo ga adha lwopomayovi omulongo (9000). Uunongononi mbuno owa hololа kutya omakuthikuthi gekakamo lyevi ngano ohaga holoka nenge tutye oga dhiingilila pehala limwe alike shono wo tashi tongola uukwatya wehala lyo, ano tashi hololа li na ehwata lyomisa dhomevi omishina dhono itaa dhi vulu okumonika nomeho, go ogo taga etitha omakakamo gevi moshitopolwa. Iizemo yomakonaakono oya ulike wo kutyaa: omahwata gomisa ngano oga taaguluka nokugoyakana nomusa omunene gokohi yevi (gwatseyika nedhina "Anker Fault") ngono gwa li gwa etitha ekakamo lyevi enene mu Apilili 2021 lyo olyo lili ekakamo lyevi enene okuholoka moNamibia li na odjundo yo5.4 M_w. Enongonono olya ulike kutja omusa gwedhina Anker Fault ogwa taandela uumbugantuzilo na ogu li tagu etitha (pakweenda kashoneelela)eyinyengo lyiipambu yevi kuya pombanda nenge pevi. Okwa dhidhilikwa ngeyi kutja momudhiingoloko mono kamu na nande efulo lyiikwamina nenge omapekaapeko gena sha niikwamina onkene kapuna ompito tayi ulike ando kutya ekakamo lyomomunvo 2018 olya etithwa kuuhasha wiilonga yomuntu, ashike otaku fekelwa omakuthikuthi gekakamo lyevi ngano taga etithwa keinyengo/ketondoko lyomeya gomevi okuziilila koothithiya dhomeya omapyu dhopopepi. Okuza momumvo omayoyi gaali nomulongo nahetatu (2018) sigo omomumvo omayovi gaali nomilongo mbali nayimwe (2021), momudhiingoloko gwaKamandjab omwa li mwa ndhindhilikwa e yo pombanda momwaalu nomoonkondo dhekakamo lyevi, shoka tashi vulu oku eta oshiponga monakuyiwa. Omapekaapeko getu otaga tula melandulathano omilandu dhoku mona mpoka puna ompito yokuholoka omakakamo gevi. Omilandu ndhika otadhi vulu woo oku longithwa miitopolwa yilwe moshilongo mwa kwatelwa naambyoka yi na iiilongitho inayi gwanena.

Auszug Im Gebiet des Kamanjab Inlier, nördliches Namibia, sind während der letzten beiden Jahrzehnte zunehmend leichte Erdbebenschwärme gefühlt worden, sowie auch einige heftigere, mit Schäden verbundene Beben. Zwischen Juni und September 2018 wurden mit Hilfe eines vom Geological Survey of Namibia (GSN) installierten zeitweiligen Netzwerks, bestehend aus zehn seismischen Aufahmestationen, ca. 1500 Bewegungen registriert. Durch Einsetzung eines auf einem neuralen Netzwerk basierenden Erdbeben-Phasendetektors (EQTransformer) wurde der GSN-Katalog auf > 9000 Erdbewegungen erhöht; zusätzlich konnten ca. 4500 der Bewegungen präziser geortet werden. Unsere verbesserte Erdbeben-Ortung identifizierte zwei größere und drei untergeordnete, deutlich unterscheidbare räumliche Ballungen, die wir als diskrete Störungen interpretieren; diese schneiden eine nach Nordosten einfallende seismogene Störung, welche verantwortlich für das M_w 5.4 Erdbeben vom 4. April 2021 ist. Das M_w 5.4 Erdbeben ist das heftigste, das jemals in Namibia instrumental aufgezeichnet wurde. Die Orientierung der von uns benannten „Anker Störung" wurde mit Hilfe des Sentinel 1 Interferometric Satellite Aperture Radar (InSAR) festgelegt, um die Verbreitung von Oberflächenhebung und Absenkung darzustellen. In Anbetracht des plötzlichen Einsetzens seismischer Aktivität, und des Fehlens von Mineral- oder Energieexploration in dem betroffenen Gebiet, schließen wir eine anthropogene Auslösung als unwahrscheinlich aus. Wir vermuten, dass die Ursache für die in Schwärmen auftretende seismische Aktivität 2018 in flachen, natürlichen Grundwasserbewegungen, die möglicherweise in Zusammenhang mit nahegelegenen heißen Quellen stehen, zu suchen ist. Im Gebiet des Kamanjab Inlier kam es zwischen 2018 und 2021 zu einem Anstieg der Anzahl und Magnitude von Erdbeben, was auf ein zukünftiges seismisches Gefährdungspotenzial hinweist. In unserer Studie stellen wir einen neuen Workflow zur Erdbebendetektion und -ortung vor, der sich für Regionen mit begrenzter seismischer Instrumentierung eignet.

Abstrak Die laaste twee dekades het die aanvang van gevoelde aardbewing-swarme gesien, met af en toe skadelike aardbewings, binne die Kamanjab-Inlier, Noord-Namibië. Die Geologiese Opname van Namibië (GSN) en Raad vir Geowetenskap, Suid-Afrika (CGS) het 'n tydelike netwerk van 10 seismiese stasies vanaf Junie tot September 2018 geplaas en ∼1500 gebeurtenisse gekatalogiseer. Ons het 'n neurale netwerk-gebaseerde

aardbewing-fasedetektor, EQTransformer, gebruik om die GSN-katalogus te verbeter tot ≥9000 opsporings en met nuwe liggings van ongeveer 4500 aardbewings. Ons dubbel-verskil aardbewegings-herplasingsresultate onthul twee hoof en drie klein onderskeidende aardbewing-ruimtelike groepe wat op afsonderlike klein verskuiwings voorkom wat die NE-duikende seismogeniese verskuiwing van die M_w 5.4-aardbewing van 4 April 2021 deursny. Hierdie M_w 5.4 aardbewing is die grootste instrumenteel opgetekende aardbewing in Namibië. Ons het verder die "Anker Verskuiwing" oriëntasie beperk deur die Sentinel 1 Interferometric Satellite Aperture Radar (InSAR) te gebruik om oppervlakopheffing en afnamepatrone te beeld. Gegewe die skielike aanvang van die seismiese aktiwiteit en die afwesigheid van minerale of energie-ontdekkingsprojekte binne 100s km, het ons die potensiaal vir 'n antropogeniese sneller uitgeskakel. Ons stel voor die oorsaak vir die 2018 seismiese swermaktiwiteit is vlak, natuurlike grondwatermigrasie wat moontlik verband hou met nabygeleë warmwaterbronne. Die Kamanjab inlier-gebied het 'n toename in die aantal en grootte van aardbewings van 2018 tot 2021 getoon, wat 'n seismiese gevaar in die toekoms kan inhou. Ons studie stel 'n aardbewingdeteksie en herlokalisering werkvloei bekend wat aangeneem kan word vir streke met beperkte instrumentasie.

Non-technical summary Residents in the Kamanjab region of northern Namibia have reported experiencing numerous, sometimes damaging, earthquakes in recent decades. We used seismic data collected by the Geological Survey of Namibia and the Council for Geoscience, South Africa, during June–September 2018, as well as satellite data and data from international earthquake networks to identify over 9000 earthquakes and locate the fault system (a group of fractures in the Earth's crust where displacement has occurred due to tectonic stresses) which generated the earthquakes. The faults are steep and run in a NNW–SSE direction, parallel to other known active faults in central and southern Namibia. There is no evidence of a correlation between these earthquakes and human activities. We suspect that natural groundwater movement played a role in triggering the 2018 earthquake swarm. The Kamanjab region has shown an increase in earthquake occurrence and intensity from 2018 to 2021. This study utilizes affordable and accessible methods to improve earthquake detection, which can help the government and communities enhance preparedness for future earthquake hazards.

1 Introduction

The Kamanjab area of Namibia (Fig. 1), a region located far from any known active faults, has instrumentally recorded moderate earthquakes ~M_w 4–6 in the last 100 years, including a M_w 5.4 normal faulting event in 2021 (U.S. Geological Survey, 2024). Felt earthquakes (M_w 3+) have been reported for decades (Fig. 2; Korn and Martin, 1950; Klein, 1980; Andreoli et al., 1996; Salomon et al., 2022; Sitali et al., 2022). Currently, an increase in detected events since 2000 is attributed to the deployment of new permanent and temporary stations by the Geological Survey of Namibia (GSN) and the Council for Geoscience of South Africa (CGS). Residents of the Anker settlement area (S -19.804030, E 14.545159; population ~600) reported an increase in felt earthquakes since the 2000s, culminating in M_w 4.8 on 14 March 2018, M_w 5.0 on 24 May 2018 and M_w 4.8 on 25 May 2018 (U.S. Geological Survey, 2024), followed by a cluster of 1500 earthquakes (M_L -1.1 to 3.6) detected by a temporary seismic network deployed by GSN and CGS between June and September 2018 (Sitali et al., 2022). The sudden increase in felt earthquakes has affected the Anker settlement and led to the relocation of Edward //Garoëb Primary School in early 2018 due to structural damage (Hartman, 24 May, 2018; Xavier and Reporter, 19 May, 2022). The continued monitoring by GSN in 2021–2022 recorded another group of moderate earthquakes (M_L 2 to 5) in 2021 (Namibian Broadcasting Corporation, 2021). These earthquakes have caused disproportionate societal impact due to lack of earthquake resilient infrastructure in the area. Unlike other moderate earthquakes in southern Africa, the intensity of the shaking is high and the shaking remains intense in large geographical areas (c.f. Midzi et al., 2013). Due to local construction methods, large infrastructure, including schools, are particularly vulnerable to shake damage (e.g. Midzi et al., 2015).

Most of Namibia is considered to be on a stable passive margin and has no known history of large earthquakes (>M_w 6, Kadiri et al., 2023), but moderate-sized earthquakes can pose serious seismic hazards for the increasing population and infrastructure in this area. The characterization of the seismicity distribution, the kinematics of fault slip, and the location and length of possible active faults has been limited by the lack of local seismic station coverage. Kamanjab is considered an active seismic zone, but specific seismogenic faults have not been defined (Kadiri et al., 2023). With this contribution, our aim is to better define the source faults responsible for earthquake swarms in the Kamanjab region and understand their triggering mechanism to explain the increase in felt seismicity over the last few decades.

To achieve this goal, we apply a multi-disciplinary approach based on a comprehensive seismicity catalog enhancement workflow to refine the spatial and temporal distribution of earthquakes reported by Sitali et al. (2022), using data from a temporary seismic network deployment between June and September 2018. We utilized earthquake phase detection, phase association, earthquake location algorithms, a double-difference relocation algorithm, magnitude estimation, and moment tensor inversion that allowed us to construct a comprehensive earthquake source parameter database for the identification of seismicity clusters and migration patterns. In total, we detected ≥9000 events in our enhanced catalog, a significant increase from the 1500 events reported in the GSN catalog. We relocated ≥4500 events and solved focal mechanism solutions for all 17 $M_L \geq 2$ events. We also applied Interferometric Synthetic Aperture Radar (InSAR) to resolve the surface displacement of the largest instrumentally recorded earthquake in Namibia, a M_w 5.4 event on 4 April 2021. We begin by outlining Namibia's tectonic settings and seis-

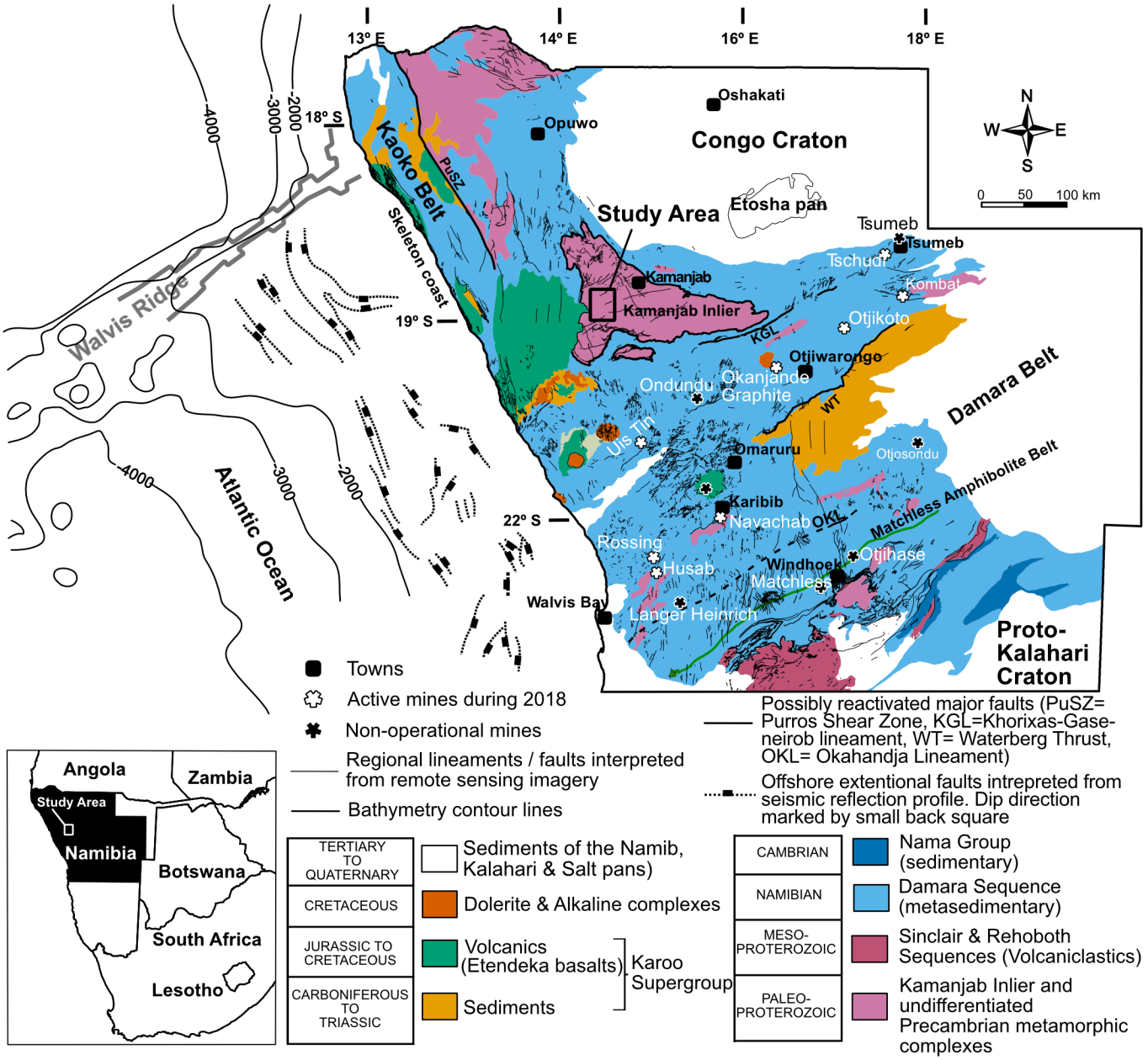

Figure 1 Simplified geology of northern Namibia (location in lower left inset) with locations of active (2017 to 2021) and recently closed mining operations (Chamber of Mines Namibia Annual Reports). There are no major energy exploration or infrastructure projects within ~150 km of the 2018 seismic swarm in the Kamanjab Inlier basement rocks near the Anker settlement. Map modified after Miller (1983); O'Connor and Duncan (1990b); Clemson et al. (1997); Konopásek et al. (2005).

motectonic history. Then, we describe the seismology and InSAR results, linking identified seismicity clusters to surface deformation. Lastly, we explore possible earthquake triggers.

2 Geological setting

2.1 Overview of the regional tectonics

Clustered seismicity occurs within the Kamanjab Inlier (KI), a ~12000 km^2 region of exposed metamorphic basement rocks including some of Namibia's oldest continental crust (Paleoproterozoic, ~2 Ga; Porada, 1979; Coward, 1981; Porada et al., 1983; Swart, 1992; Prave, 1996; Jelsma et al., 2018). The crystalline rock is surrounded by younger (Mesoproterozoic to Cambrian) sediments of the Damara and Nama Groups (Miller, 1983; Becker et al., 2006). The two billion-year history of these rocks implies the potential for structural inheritance that could affect present-day seismicity. These crystalline rocks comprise highly deformed granitic gneiss, metasediments, and intrusive rocks (Fig. 1, pink). The upper layers of the basement are the extensive low-grade metamorphosed Damara Group marine sedimentary platform rocks, predominantly carbonates, that transition to clastic sediments farther south (Fig. 1, blue; Coward, 1981; Miller, 1983). These rocks were deformed during the regional collision of the Congo, Kalahari, and Rio de Plata cratons (Brazil and Uruguay) during the Neoproterozoic (Martin and Porada, 1977; Lehmann et al., 2016). These collisions were responsible for the formation of the intersecting

NNW-trending Kaoko and ENE-trending Damara orogenic belts in northwestern and central Namibia, respectively (Fig. 1).

The final widespread structural events affecting the region were associated with late Paleozoic-Mesozoic Atlantic rifting and the intrusion of Karoo sills and dykes in the Jurassic (Miller, 1983). At ∼130 Ma, the breakup of the western Gondwana supercontinent and the opening of the Atlantic Ocean gave rise to the NNW-striking, vertical to west-dipping extensional faults along the continental margin (Clemson et al., 1997; Passchier et al., 2002). The thick Etendeka flood basalt, interpreted to have risen from the Tristan da Cunha hotspot associated with the spread on the Walvis Ridge at 70 Ma (O'Connor and Duncan, 1990a), blankets and intrudes the Kaoko belt.

Most of the Proterozoic structural features in the KI were overprinted by the ∼660–550 Ma Damara Orogen (Konopásek et al., 2005) and rotated in parallel with the Kaoko and Damara belts. These are apparently not associated with continental shelf structures formed during rifting at ∼130 Ma. The Proterozoic and Pan-African (Neoproterozoic-Cambrian) faults have not been associated with any field evidence for paleoearthquakes (for example, recent fault scarps or co-seismic frictional melts; pseudotachylyte) or precise locations of historical earthquakes (e.g. Korn, 1951; Mangongolo et al., 2008; Geological Survey of Namibia, 2009).

2.2 Seismotectonics in Namibia

Namibia's large-scale faults and lineaments have been mapped in detail through regional geological mapping (e.g. Geological Survey of Namibia, 2009; Pickford, 2023) and aeromagnetic interpretation (e.g. Corner and Durrheim, 2018). Considering the widespread mining and mineral exploration activity in Namibia, there is potential for anthropogenically induced earthquakes (c.f. Foulger et al., 2018). Recent reactivation of NE-trending major crustal scale structures, interpreted to have formed in a compression regime, has been suggested (e.g., on the Omaruru Lineament-Waterberg Thrust and Okahanja Lineaments; Raab et al., 2002), but only rare seismic events have been recorded on these structures (c.f. Korn, 1951; Klein, 1980; Salomon et al., 2022; Muir et al., 2023).

Known active faults are found onshore and offshore parallel to the coastline and on the Walvis Ridge (Fig. 1, Fig. 2a). Most of onshore seismicity is linked to the Pleistocene to recent faults that offset the Cenozoic to Quaternary basins. The most notable paleoseismic onshore faults are the Hebron (Andreoli et al., 1996; White et al., 2009; Salomon et al., 2022), Tsau ǁKhaeb, and Hai-s faults (Muir et al., 2023) in southwest Namibia. The faults were seismically active during the Pleistocene, preserving records of multiple surface-rupturing earthquake cycles in the range of M_w 6–7 (Salomon et al., 2022; Muir et al., 2023). The Hebron, Tsau ǁKhaeb, and Hai-s faults remain the only well-studied paleoseismic faults in the country. The scarcity of paleoseismic studies allows for the possibility of many recently active faults yet to be discovered.

Evidence for pre-Cretaceous and recent faulting has been identified on the continental shelf in southern Namibia, using bathymetric and seismic reflection data collected for diamond exploration. Kirkpatrick and Green (2018) reported NNW-striking recent fault scarps striking the NNW that control sediment accumulation north of the Orange River on the southern border of Namibia, but considered them inactive because they do not cut the modern seafloor. In contrast, Viola et al. (2005) reported mud volcanoes along NNW-trending lineaments interpreted as active faults in spite of no documented seismicity, but this is also explained by the lack of instrumentation. The seismic potential of the middle Pleistocene to recent faults in the central part of the Damara belt, ∼240 km southeast of the KI (Fig. 2a), was assessed by previous workers (Korn and Martin, 1950; Korn, 1951; Klein, 1980). Most of these faults are reverse and parallel to the NE–SW striking Damara belt, offsetting the calcrete-cemented terraces in the Omaruru River (Fig. 1). These scarps indicate recent reactivation, consistent with historic earthquakes that caused shaking intensity up to V on the Mercalli scale (Korn and Martin, 1950).

Offshore seismic swarms and volcanic eruptions recorded in Walvis Ridge (Fig. 1) are attributed to the active magmatic system (Haxel and Dziak, 2005). These inferences are not compatible with previous claims (e.g. O'Connor and Duncan, 1990b) that the ridge has been inactive since it was produced by a Mesozoic plume and raise questions of whether continued activity might be driven by dextral strike-slip in smaller fracture zones within the Walvis Ridge (Haxel and Dziak, 2005).

We still lack information about the source mechanisms for on- and offshore earthquakes, as well as how the seismically active Walvis Ridge intersects the continental margin. Given the vast differences in tectonic history and the large distances from the KI to all known seismogenic structures, it is unlikely that these structures extend into the KI. However, continued tectonic activity suggests a strong role for structural inheritance that affects modern seismic hazard in coastal Namibia.

2.3 Kamanjab Inlier Earthquake Swarm

The Namibian earthquake detection capabilities have improved significantly with upgrades and expansion of the national seismic network since the early 2000s (Mangongolo et al., 2008). According to International Seismological Center, only the Windhoek (WIN) and Tsumeb (TSUM) stations (Fig. 2a) have been continuously operational since 2000. In addition, the Namibian Geological Survey retains data from additional stations, including Kamanjab (KJAB), Opuwo (OPU), and Rundu (RUDU) located within 600 km of the Anker settlement (Fig. 2a), have been operational and recorded data locally since early 2009. Although these data are included in the GSN catalog, they have not been uploaded to the public domain (e.g. International Seismological Center) due to poor remote network infrastructure. Most cataloged earthquakes within Namibia are concentrated in the central part of the country, consistent with the denser distribution of stations in this region compared

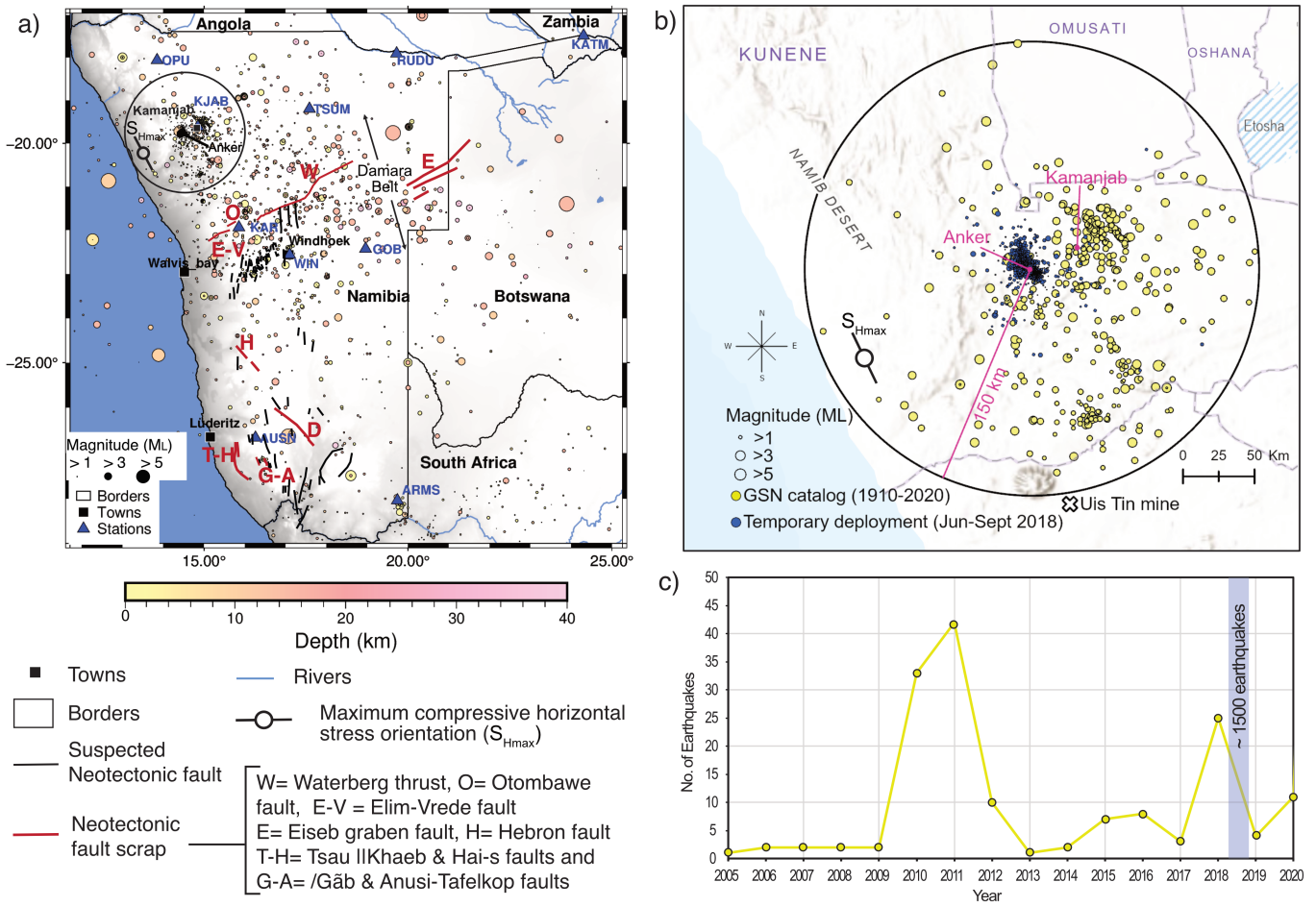

Figure 2 a) Distribution of historical earthquakes M≥1 (color indicates depth, symbol size scales with event magnitude) in Namibia and neighboring countries from 1910–2020 from the Geological Survey of Namibia Earthquake catalog 1910 to 2020. Neotectonic fault scarps (red solid lines) and lineaments (black solid lines) in Namibia, from Korn (1951); Viola et al. (2005); Salomon et al. (2022); Muir et al. (2023). The maximum horizontal stress orientation for normal faulting is trending NW–SE (Viola et al., 2005; Heidbach et al., 2016, 2018). b) Topographic shaded relief map (source: ESRI ArcGIS) showing the concentration in earthquake activity within 150 km (black solid circle) of Anker settlement recorded by Namibian seismic stations. c) Graph depicts annual number of catalog events between 2005 and 2020 (Geological Survey of Namibia Earthquake catalog 1910 to 2020), excluding the 1500 events from the 2018 temporary deployment (Sitali et al., 2022), there is still an increase in recorded events in most years since 2009. Note that the 150 km zone is delineated to exclude the Uis Tin Mine, which commenced operations in late 2019.

to the rest of the country (Fig. 2a, b). Thus, station distribution within 150 km of the Anker settlement does not explain the increases in seismicity beginning around 2009 (see the line graph, Fig. 2c).

A sudden increase in felt earthquakes and building damage in the KI near the Anker settlement in early 2018 motivated the deployment of 10 temporary stations between June and September 2018 by the Namibia Geological Survey and the South African Council for Geoscience, which recorded more than 1500 (M_L -1.1 to 3.6) events (Fig. 2b) during the deployment (Sitali et al., 2022). After decommissioning the temporary network, the sparsely distributed permanent stations detected a few small to moderate earthquakes in the same area, including a M_w 5.4 earthquake on 04 April 2021. The closest permanent Kamanjab station (KJAB) is located approximately 40 km northeast of the study area. The station should be capable of detecting small local earthquakes ($M_L \geq 2$) within the 50 km radius, although the catalog may still miss smaller magnitude events due to the challenges of single-station event detection, so the event counts after September 2018 represent a minimum estimate.

No major infrastructure or energy production projects (e.g. dams or mining) with the potential to induce earthquakes were observed within 30 km of the seismicity during field visits. According to annual mine reports (Chamber of Mines Namibia Annual Reports; Geological Survey of Namibia Online Database, 2024), there is no active mining or exploration activity within 150 km of the swarm near Anker (Fig. 1) from 2017 to 2021. The closest significant development, Uis Tin, is over 150 km from Anker settlement, and only began operating in 2019. Consequently, anthropogenic triggering was ruled out as a source of the events. In the absence of potential anthropogenic causes, the sudden onset of earthquake swarm activity in the KI presents an opportunity to investigate natural proximal causes of intraplate earthquake swarms.

Sitali et al. (2022) showed that most of the seismic

events in the cluster were located around the Anker settlement (Fig. 2b). The event depth profile (see Fig. 6 in Sitali et al., 2022) displays two main clusters, a shallow cluster in the east between 0 and 20 km and a deeper cluster in the west between 10 and 25 km, and both clusters are interpreted as dipping west. Sitali et al. (2022), calculated focal mechanism solutions for M_L 0.1–1.5 events between 21–28 June 2018, tallying 18 normal faults, 10 reverse faults, and 5 strike slip faults. These focal mechanism solutions were compared with the regional lineaments mapped from aeromagnetic data, but this approach was not conclusive in linking the earthquakes with any specific lineament or structure. Furthermore, Namibia's aeromagnetic data were acquired at a line spacing of 200 m with 2500 m ties and a nominal terrain clearance of 80 m (Hutchins and Wackerle, 2007). This resolution incorporates spatial uncertainty, which could have led to significant errors in interpreting lineaments, the location of seismicity, and the association of seismicity with faults.

We build on the work of Sitali et al. (2022) by employing a multidisciplinary approach that combines machine learning algorithms to enhance the seismicity catalog, and focal mechanism solutions and InSAR to identify the potential active faults. Using these high-precision tools, we aim to contribute to understanding of the mechanisms of the origin of the earthquake, assess the seismic hazards in the region, and support the case for expanding the seismological observation capacity in Namibia.

3 Methods

3.1 Catalog enhancement and relocation

Enhancing earthquake catalogs is of utmost importance to identify previously unmapped but seismically active faults and to address the challenges associated with detecting and characterizing smaller events, especially in the presence of a low signal-to-noise ratio (SNR) for conventional methods such as STA / LTA (short-term average to long-term average ratio) and template matching (Trnkoczy, 2009; Chamberlain et al., 2018). We developed a workflow to overcome these challenges and improve seismicity catalogs by leveraging machine learning tools. Our workflow consists of: (1) automatic earthquake phase detection based on a multitask deep neural network, (2) event association using phase pick numbers and travel time residuals, and (3) initial event location determination using a maximum likelihood method followed by double-difference (DD) relocation. To evaluate the robustness of the workflow, we implemented a comprehensive quality control process to ensure the accuracy of the machine learning catalog. This process included waveform inspections (refer to Supplemental Figures S1, S2 and S3) and hyperparameter tuning.

3.1.1 Machine Learning Phase Pick

We apply EQTransformer, a deep neural network that incorporates an attention mechanism that is utilized as the foundation of an artificial intelligence-driven system to detect earthquake signals and pick the P and S phases (Mousavi et al., 2020). Next, we reinforced our phase pick detection using Siamese-EQTransformer, which applies a secondary template matching by the Siamese neural network to reduce the false negative rate of EQTransformer, retrieving previously missed phase picks in low SNR seismograms based on similarities to phase picks from the pre-trained EQTransformer model (Xiao et al., 2021). More details of the parameters used are provided in the Supplemental Material Text S1.

3.1.2 Phase Association

To associate phase picks to identify individual earthquakes, we use the newly developed phase association tool, PyOcto (Münchmeyer, 2023), which offers flexible parameter options and fast computation. Furthermore, Münchmeyer (2023) benchmark results demonstrate that PyOcto outperforms other popular associators in two synthetic scenarios and the 2014 Iquique aftershock sequence. In this step, we use PyOcto to associate seismic P- and S-wave phase picks with earthquake events using a 4D space-time grid search technique based on the number of phase picks and residual travel times calculated from a one-dimensional velocity model for our study area (Midzi et al., 2010), which is used as a starting velocity model in Sitali et al. (2022). In our implementation, we did not adopt the updated velocity model computed by Sitali et al. (2022) using VELEST (Kissling et al., 1994), which performs a simultaneous inversion for the velocity and hypocenter parameters. This decision was informed by our observation that the coordinates of Station ST8 used in the Sitali et al. (2022) velocity inversion were offset by approximately 20 km from its actual location, therefore probably resulting in systematic biases in the updated velocity model. As a result, we opted to use (Midzi et al., 2010) model which is the closest velocity model available for our field area (See Supplemental Table S1). To minimize false detections, we established a minimum threshold requiring that an event must be recorded with both P and S phase picks at no fewer than four stations, amounting to a total minimum of eight phase picks for a single event.

3.1.3 Initial Location and Relocation

In this study, we applied the NonLinLoc package, which incorporates a maximum likelihood location method (Lomax et al., 2014), to obtain the initial earthquake locations. The NonLinLoc package is a comprehensive set of software tools designed to calculate travel times through 3D grid cells constructed from 1D or 3D velocity model, and conduct probabilistic, non-linear, and global-search earthquake locations in 3D structures. To further refine our location results, we applied the double-difference (DD) hypocenter location algorithm HypoDD (Waldhauser and Ellsworth, 2000), which is based on two assumptions to enhance the accuracy of hypocenter determinations. Firstly, it presumes that the separation between the hypocenters of two earthquakes is significantly smaller than the distance from

the earthquakes to the seismic stations and the scale of heterogeneities in seismic velocity. Secondly, the technique assumes that the seismic ray paths from the earthquake source region to a given station are almost identical for closely spaced events. In such cases, the disparity in travel times observed at a single station between two events can be attributed to the precise spatial offset between the events (Frechet, 1985).

The double-difference technique enables the combination of conventional phase picks from earthquake catalogs and/or high-precision differential travel times derived from the phase cross-correlation of P- and/or S-waves. For catalog travel-time differences, a maximum of 200 neighbors per event and a minimum of 8 links are required to define a neighbor. A 2-second window was used for both P and S phase cross-correlation, with a threshold of 0.70. A minimum threshold of eight travel-time observations in event pairs and a maximum separation threshold of 20 km (catalog) and 2 km (cross-correlation) were used as criteria for event pair relocation. We employ these distance parameters because the catalog travel time differences provide a large-scale picture, while the event pair cross-correlation travel time difference resolves the structure on the scale of individual earthquakes (Waldhauser and Ellsworth, 2000). Approximately 50% of the selected events met the criteria using both types of travel time measurement.

After the relocation process, the data set was grouped into distinct clusters using the DBSCAN algorithm (Density-Based Spatial Clustering of Applications with Noise) in three dimensions (latitude, longitude, and depth). DBSCAN, as introduced by Ester et al. (1996), identifies high-density regions and separates them from lower density areas. Unlike traditional clustering methods such as K-means (MacQueen, 1967), DBSCAN does not require specifying the number of clusters in advance, and it can discover clusters of arbitrary shapes, as well as identify outliers. The algorithm relies on two main parameters: the maximum distance between two samples to be considered neighbors (ϵ) and the minimum number of neighboring points required to form a cluster (*min_samples*). Through empirical testing of various parameter values, we found that setting $\epsilon = 0.0018$ and *min_samples* $= 45$ produced the most meaningful clustering results, as indicated by a Silhouette Score (Rousseeuw, 1987) of 0.698. By definition, the Silhouette Score ranges from -1 to 1. Scores above 0.5 generally indicate good clustering, while those above 0.7 are often considered near-perfect. We also visualized the resulting cluster patterns for confirmation. Using these parameters, the algorithm identified five distinct clusters within the dataset. Additionally, we performed a Fourier transform (FFT) analysis (Harris, 1978) on our event catalog to investigate the periodicity variation of events records in our catalog (discussed in more detail in 5.3)

3.1.4 Magnitude estimation

We defined the local magnitude as $M_L = \log_{10}(A) + 1.149\log_{10}(R) + 0.00063R + 2.04 - S$ (where A is the maximum amplitude, R is the hypocentral distance from event to station in kilometers and S is a station correction term). The coefficients were empirically derived by Saunders et al. (2013) using analyzed synthetic Wood-Anderson seismograms recorded by the South African National Seismograph Network between 2006 and 2009 (Saunders et al., 2013), and the station correction term (S) was determined form the regression analysis of the ten temporary GSN stations, generating values ranging from -0.31 to 0.32.

3.2 Focal Mechanism Solution

We utilized open-source Python software Grond (Heimann et al., 2018) to estimate focal mechanism solutions (FMS) for relocated earthquakes with M_L > 2.0. Grond employs a Bayesian bootstrap probabilistic joint inversion scheme, simultaneously fitting six independent moment tensor components, seismic moment, centroid location, and origin time, as well as their uncertainties. This scheme is well suited for small events and can offer a complete understanding of the interaction between parameters for further testing (Kühn et al., 2020). In our study, we employ a combination of time-domain full waveforms, time-domain cross-correlations, frequency-domain amplitude spectra, and envelope analyses of time-domain waveforms as input for inversion. Specifically, misfits between fully inverted waveforms and modeled data sets are combined using an L1 or L2 norm, and different stations are automatically weighted to account for variations in epicentral distances.

The initial inversion step involves calculating Green's function database using a regional 1D velocity profile and a 3D grid of potential hypocenters. Additional programs, Qseis (Wang, 1999) and Fomosto (Heimann et al., 2019), are used for Green's function computation. Based on the relocated catalog depth range and station distribution, we set a grid spacing of 200 meters for both horizontal and vertical dimensions, with a maximum horizontal distance of 300 kilometers and a source depth ranging from 1 to 20 kilometers. To maintain fidelity, we utilized a sampling rate of 10 Hz for the synthetic Green functions, accounting for the full waveform fitting range from frequency 0.01 to 5 Hz.

Next, we employ various time windows, ranging from 1 s before the P-phase arrival to 5 s after the S-phase arrival, to compare observed waveforms to synthetic waveforms constructed from the Green functions in all three components. This time range is primarily determined by the event-station travel time, taking into account station distances ranging from 1 to 70 kilometers, to ensure comprehensive coverage of event waveforms. To identify the parameter set that yields the lowest global misfit, we conduct 5000 iterations of several different inversions using different frequency bandpass filters. The tested frequency bands generally fall within the range of 0.05 to 4 Hz, following previous studies that investigated similar magnitude events and source-station distances (López-Comino et al., 2021; Petersen et al., 2021). Through a trial and error process, we select a frequency band of 1.5–3 Hz and subsequently perform a total of 60000 iterations for each event to accom-

modate the processing time, misfit decreasing and stabilizing (see Supplemental Figures S4 and S5 for more detailed waveform fitting and misfit examples).

3.3 Interferometric Synthetic Aperture Radar

In order to test for and locate any surface deformation caused by the recent seismicity within the Kamanjab Inlier, we produced interferograms for several of the largest earthquakes, which were most likely to have produced a detectable signal. This includes the M_w 5.0 event that occurred on 24 May 2018 and the M_w 5.4 earthquake that occurred on 04 April 2021. Initially, we processed 12-day co-seismic interferograms for both events, using Sentinel-1B imagery and the GMTSAR software package (Sandwell et al., 2011). As no descending track images are available for this region (ESA, 2024), we were limited to producing interferograms along the two ascending track orbits, numbers 29 and 131, that covered the earthquake locations.

Our initial data processing with the limited co-seismic interferograms did not show any significant tectonic surface deformation signals. However, small tectonic signals may have been obscured by atmospheric and spatio-temporal decorrelation noise. In order to better account for this, we constructed an InSAR time series using a coherence-based Small BAseline Subset Analysis (SBAS) (Berardino et al., 2002; Schmidt and Bürgmann, 2003; Tong and Schmidt, 2016; Trnkoczy, 2009; Xu et al., 2017) that utilizes common point stacking to remove decorrelation noise. SBAS enables surface deformation to be observed in high-order spatial and temporal resolution, allowing the tectonic signals to be reconciled. This method has been widely used in various geodetic fields, including studies of ground subsidence, landslides, and seismic activity (Li et al., 2022).

The 24 May 2018 M_w 5.0 event occurred prior to the installation of the GSN-CGS temporary seismic network from June to September 2018. The time series for this event comprised 40 interferograms and covered the period 7 May to 28 September 2018, capturing the coseismic deformation associated with the M_w 5.0 earthquake and the swarm of seismicity that was recorded during the temporary network deployment. The M_w 5.4 earthquake on 4 April 2021 was the largest earthquake recorded by modern instruments in Namibia. The time series for this event was constructed for the period from 4 March to 31 August 2021 and included 67 interferograms. Interferogram pairs were selected using a temporal baseline of 50 days and a perpendicular baseline of 100 m. The short temporal baseline was set in order to resolve seasonal changes from affecting the time series (Xu et al., 2017).

We also analyzed the potential for fault scarps which might indicate recent faulting using Google Earth imagery, followed by a ground-truth survey in April 2022. However, most of the surface was covered by vegetation during our ground survey, making it difficult to identify any signs of active faulting or surface deformation indicated by the InSAR signal.

4 Results

4.1 Machine Learning Catalog and Relocated Seismicity

We applied the machine learning (ML)-based catalog enhancement workflow over an area of about 400 km^2, including the Anker settlement (near ST9; Fig. 3a). We used data recorded by ten temporary stations from 10 July to 24 September 2018, which differs from the catalog of Sitali et al. (2022) that starts in late June because 6 of 10 stations started to operate on 10 July 2018. However, we expanded the existing catalog (Sitali et al., 2022) of ~1500 events to nearly ~9000 events (Fig. 3b). The nearly six-fold increase in the number of detected events, mostly of magnitudes lower than 1, suggests that this area is more seismically active than previously known.

Figures 3c and 3d illustrate that the station network was capable of detecting seismic events with local magnitudes as low as M_L -1, and the majority of the detected events ranged from M_L -0.3 to 1 (Fig. 3d). In particular, the aftershocks of the three largest events included some events of M_L 2, M_L 3.34 on 30 July 2018, M_L 2.9 on 12 August 2018, and M_L 2.91, on 24 August 2018 (Fig. 3c). On average, ~100 events were recorded daily, some days recording more than 200 events (Fig. 3b).

We investigated the decay characteristics of the aftershock rate following Omori's law for the largest event, M_w 5.0, on 24 May 2018. As depicted by the colored dashed line in Fig. 3b, the aftershock frequency follows Omori's formula, $n(t) = \frac{k}{(c+t)^p}$, characterized by the different assumption of the first-day aftershock number k and decay rate parameter p, fixed constant to avoid singularity $c = 0.01$ (Omori, 1895). Since our data set begins 47 days after the main shock, it is difficult to accurately determine the number of the first-day aftershock k. However, the decay rate of $p = 0.64$ and $p = 0.48$ is significantly lower than the typical empirical rates of p (approximately 0.9 to 1.1) when we assume the first-day aftershock number is 2000 and 1000, respectively. These small decay rates with the potential overestimated aftershock number indicate a swarm-like activity pattern (c.f. Parsons, 2002; Shcherbakov et al., 2004). Additionally, we assessed model performance by computing the coefficient of determination, R^2, over a parameter grid $p \in [0.1, 2.0]$ and $k \in [500, 20000]$ (see Supplemental Figure S6). The maximum $R^2 \approx 0.20$ shows that the Omori model explains only 20% of the variance in the daily counts, highlighting the challenge of fitting aftershock decay at longer periods after the mainshock. Nevertheless, the best fits occur within the range of $p \in [0.5, 0.8]$ and $k \in [500, 7500]$, which remains consistent with a swarm-dominated sequence punctuated by small earthquakes and their aftershocks.

Further evidence of swarm-like events is observed in Fig. 3d. It is common for earthquake swarms to exhibit b-values significantly greater than 1.0 (Jenatton et al., 2007; Minetto et al., 2022). In our study, b-value of 1.277 with an uncertainty of 0.014 is calculated using:

$$b = \frac{\log_{10} e}{\overline{M} - \left(M_c - \frac{1}{2} M_{\text{bin}}\right)} \quad (1)$$

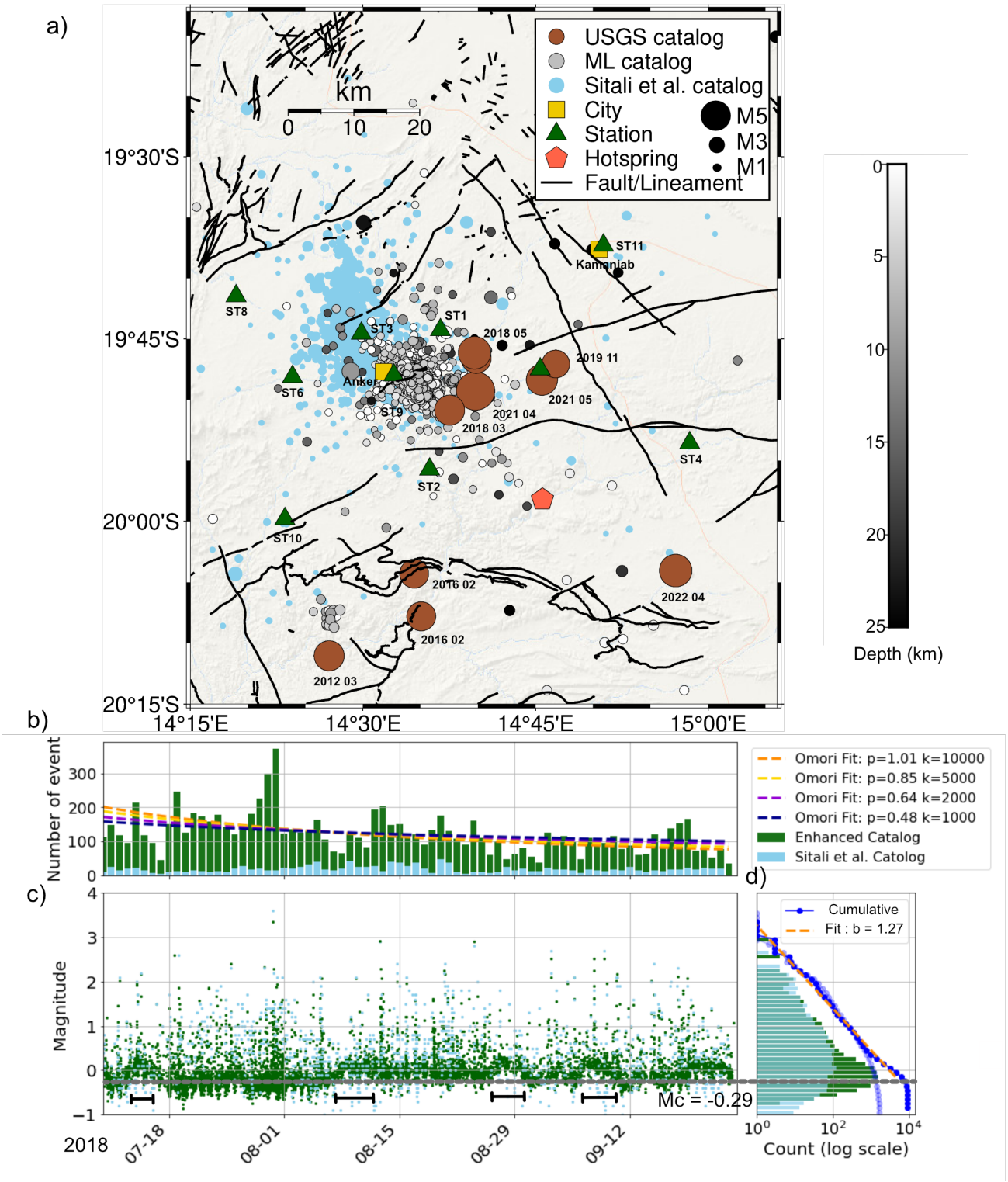

Figure 3 a) Earthquake locations from a machine-learning-enhanced catalog (ML catalog), capturing ∼9000 events (grayscale colorbar for depth) from 10 July to 24 September 2018. Green triangles = location of Geological Survey of Namibia temporary stations (ST1 to ST11). The initial event locations from Sitali et al. (2022) are shown as sky-blue circles. Dark red circles show US Geological Survey epicenters of regional earthquakes. The black solid lines represent undifferentiated geological lineaments (Geological Survey of Namibia, 2009). Kamanjab (population ∼6000) and Anker (population ∼600) are indicated by the yellow squares. b) Daily number of events from the ML catalog (green bars) and from Sitali et al. (2022) catalog (sky blue bars), 10 July to 24 September, 2018. The colored dashed line represents Omori's law, which best fits with a decay rate of p since the M_w 5.0 on 24 May 2018, with the different assumptions of first-day aftershock numbers k. c) Event magnitude distribution. Highlighted black intervals in c) mark periods where all events exceed M_c. Fitting to the Sitali et al. (2022) catalog gives M_c near 0.38 and b-value 0.88 (blue transparency cumulative curve and Figure S6). d) Magnitude-frequency distribution, fitted using the maximum likelihood method (Aki, 1965), yields a b-value of 1.19 and a completeness magnitude M_c of -0.22 (gray dashed line) in ML catalog.

(Aki, 1965; Iwata and Nanjo, 2024), where $\overline{M}$ represents an average magnitude in the catalog, M_c is the completeness magnitude ($M_c = -0.29$ for all earthquakes in the ML-based initial catalog; Supplemental Text S2 and Figure S7), and $M_{\text{bin}} = 0.1$ is the magnitude bin width used for fitting cumulative values, and the uncertainty is estimated as the standard deviation of 1000 bootstrap replicates (Supplemental Figure S8). Compared to Sitali et al. (2022) catalog, where M_c is approximately 0.38 and the b-value is 0.88 $\pm$ 0.065 (see Supplemental Figure S9), our new ML-based catalog has a lower detection threshold and hence a more complete record of seismicity (Fig. 3d). However, as noted in Section 3.1.2, their magnitude estimates involve considerable uncertainties due to station location offsets in the catalog enhancement process. In addition, we also observed several intervals where all catalog events have a magnitude over M_c (Fig. 3c, time intervals indicated with black bracket). Furthermore, 95% of the seismic activity was concentrated around the Anker settlement (Fig. 3c, yellow square), within a radius of up to 10 km (see Supplemental Figure S10 for additional details).

To further validate that our enhanced detections are true earthquakes instead of false positives, we inspected the waveforms of all events detected on the following three dates: 1) 30 July, the day with the highest number of detections, 2) 5 August, the day with a burst of events with a wide range of magnitudes from -0.5 to 2.1 (Supplemental Figure S11), and 3) 27 August when there was a M_L 3.0 with several episodes of M_L ~1.5 events (Supplemental Figure S12). We examined the relationship between these events (around 600 events) and the distances between the stations and the estimated epicenters alongside the phase picks generated by EQTransformer (see Supplemental Figures S1–S3 and Movies S1–S3). Through careful visual inspection, we found that over 97% of these events exhibit a robust correlation between the phase pick travel time sequences and their distances from the stations. This suggests high reliability in the phase picks plus phase association, where any questionable phase picks or events are earmarked for exclusion in the forthcoming relocation process.

Using HypoDD (Waldhauser and Ellsworth, 2000), we first estimate the maximum expected delay time—the interval required for P- and S-waves to travel between two events—based on the preliminary locations and a velocity model specifying P- and S-wave velocities of 4.0 and 2.3 km/s, respectively, in the focal region. To account for uncertainties in the initial locations, we include a 0.5-second margin. Consequently, any delay time exceeding this threshold for a given event pair is considered indicative of an erroneous detection.

The distributions of location uncertainties for both the initial ML catalog and the relocated catalog are shown in Supplemental Figures S13 and S14, indicating approximate uncertainties of 1 km and 100 m, respectively. More importantly, comparisons between the relocation event distributions (Figures 4a, b, and c) and the initial ML event distributions (Figure S15) reveal a more pronounced linear structure and a clearer clustering after relocation.

The NE–SW striking lineament co-located with the seismicity (Figures 3a and 4a) near ST9 was investigated briefly during a field visit and was found to be a ~2.5 m thick deformed quartz vein striking ~216° and dipping ~68°NW. No kinematic indicators or other evidence of shear displacement was found that could suggest recent faulting on this structure. Furthermore, the GSN database (Geological Survey of Namibia, 2009) for regional lineaments (Fig. 3a) lacks fault kinematics information, so it does not differentiate faults from other fractures nor indicate the age of the fractures. However, the two major regional trends in the lineament database offer a basis for comparison to our earthquake distribution and surface deformation associated with the 2018 and 2021 mainshocks (discussed in more detail in Section 4.3).

Following the relocation of approximately 4500 seismic events (as discussed in Section 3.1.3), we grouped the events into five distinct clusters using the 3D DBSCAN method. Fig. 4a illustrates that the majority of these clusters are located near the Anker settlement and ST9 station, and aligned along a northwest-southeast axis. This near-elliptical shape in event clustering with a long axis oriented NW–SE aligns with the focal planes for the largest events (Fig. 4a and d) and is consistent with the maximum horizontal stress inferred for southwestern Africa (e.g. Andreoli et al., 1996; Viola et al., 2005; Heidbach et al., 2018), and indicated in Fig. 2b. However, correlating the spatial distribution of seismic events with the NW–SE trending geological lineaments in the region (plotted in Fig. 3a) remains inconclusive since no previously mapped NW–SE striking structures intersect the relocated seismicity.

The cluster analysis reveals spatial clusters of the nearly 4,500 events, mainly in Cluster 1 (2016 events at depths of 5–6 km), Cluster 2 (1171 events at depths of 2.5–4.5 km), and Cluster 3 (1099 events at depths of 3–5.5 km). The hypocenter shapes of the clusters range from equant (cluster 1) to elongated ellipsoid (clusters 2–5) with long axes that apparently plunge steeply between north and northeast in different profiles (Fig. 4b, c and Supplemental Figure S16). The hypocenter of clusters 1–4 make up a tabular zone striking NNW and dipping ~70° to the ENE, which we have interpreted to represent the fault geometry. Cluster 5, comprising roughly 100 events, is located at shallower depths between 1–2.5 km and approximately 1.5 km east of Cluster 1 (Fig. 4a, b, c). Meanwhile, Cluster 4, which contains fewer than 50 events, is at a deeper depth of 6 to 7 km and with epicenters located at 0.5 to 1 km NW of Cluster 3 (Fig. 4a, b, c). Cluster 5 is situated at a considerable distance from the other clusters, and we interpret it as a branch of the primary fault. A three-dimensional plot and movie can be found in Supplemental Figure S16 and Movie S4, respectively).

Fig. 5a shows the daily event counts of the relocated events for each cluster. The hatched bars indicate days on which the number of events exceeds the mean plus 1.5 standard deviations for that cluster, corresponding to approximately the top 6.68% of a normal distribution (see Supplemental Table S3 for details). These anomalous dates include 19, 21, 29, 30, and 31 July 2018; 5,

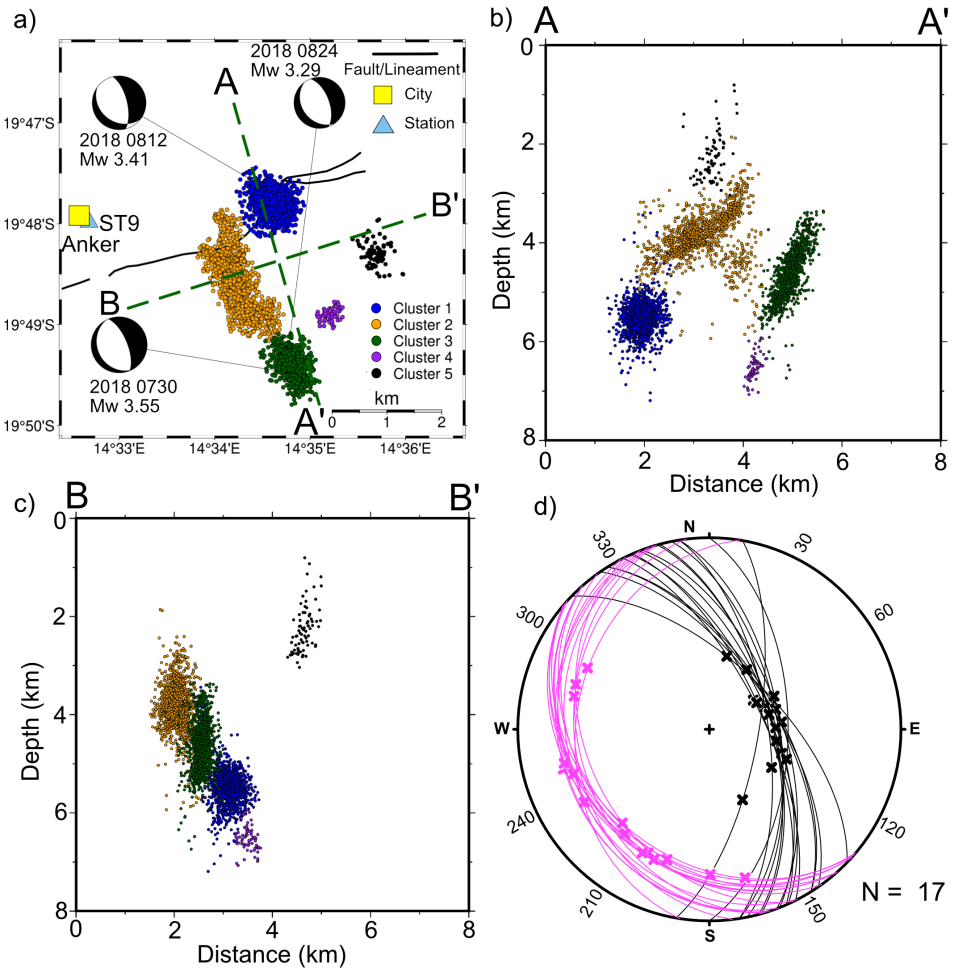

Figure 4 a) Epicenters of five relocated clusters and focal mechanism solutions (FMSs) of the three largest earthquakes M_w 3.55, M_w 3.41, and M_w 3.29 (M_L = 3.34, 2.9, and 2.91, respectively) recorded during the deployment. The black solid lines represent NE–SW striking faults (Geological Survey of Namibia, 2009) that were briefly investigated in the field and showed no evidence of active faulting. Daily event distribution can be found in Supplemental Movie S5. b) Depth cross-section of clusters projected along AA' NNW–SSE direction. c) Depth cross-section of clusters projected along BB' WSW-ENE direction. d) The lower hemisphere equal-area (Schmidt net) using Stereonet (Allmendinger et al., 2011) showing two fault plane solutions (black solid lines and magenta solid lines), and slip vectors (magenta and black crosses) from all ($N = 17$) calculated FMSs. The NE-dipping nodal planes correlate with NNW–SSE striking and NE-dipping orientation of the event clusters shown in a and c, and we interpret this orientation to represent the fault geometry.

12, 13, 14, 20, and 24 August 2018; and 10, 15, 17, and 19 September 2018. Generally, there is no overlap in high-activity periods between the clusters, except on 31 July 2018 when both clusters 2 and 3 exhibited more seismic activity. However, when Cluster 1 (blue) exceeds its mean plus 1.5 standard deviations, Cluster 3 (green) remains below its average, typically by approximately 0.5 standard deviations (see Supplemental Table S4). Furthermore, considering the highest magnitudes (relocated events) on these anomalous dates in Clusters 1 and 3, we observe a negative correlation (coefficient of -0.72, p-value $= 0.0083$), indicating an anti-correlation with a confidence of approximately 99% (see Supplemental Table S4 and Figure S17).

Furthermore, we estimated the b-values in the three main clusters (Clusters 1, 2, and 3) using the maximum likelihood method as described in Equation 1. To enhance the robustness of the statistical fitting and mitigate biases from significantly large or small events, we employed a sliding window approach with a window size of 200 events and a step size of 50 events with uncertainties evaluated through 1000 bootstrap iterations (Fig. 5b, c, and d). We also present the variation of M_c for each sliding window in (Fig. 5e). The data points correspond to the midpoints of each time interval used in the b-value calculations. Additionally, dashed lines highlight periods when events with $M_L > 2.0$ occurred, with colored dashed lines indicating cluster categorizations for relocated events and black dashed lines representing events not relocated by HypoDD (see Supplemental Table S5 for detail information).

In Cluster 1, the b-value fluctuation closely follows the occurrences of large events (M_L > 2.0). Both b and M_c declined between 14–21 July 2018 due to aftershocks of the $M_L = 2.17$ on 14 July and $M_L = 2.6$ on 18 July in Cluster 1 (Fig. 5a, b and e). The b-value then rose to ~1.3 after 21 July alongside an increase in M_c. A similar jump from ~0.8 to 1.3 followed the $M_L = 2.9$ on 12 August,

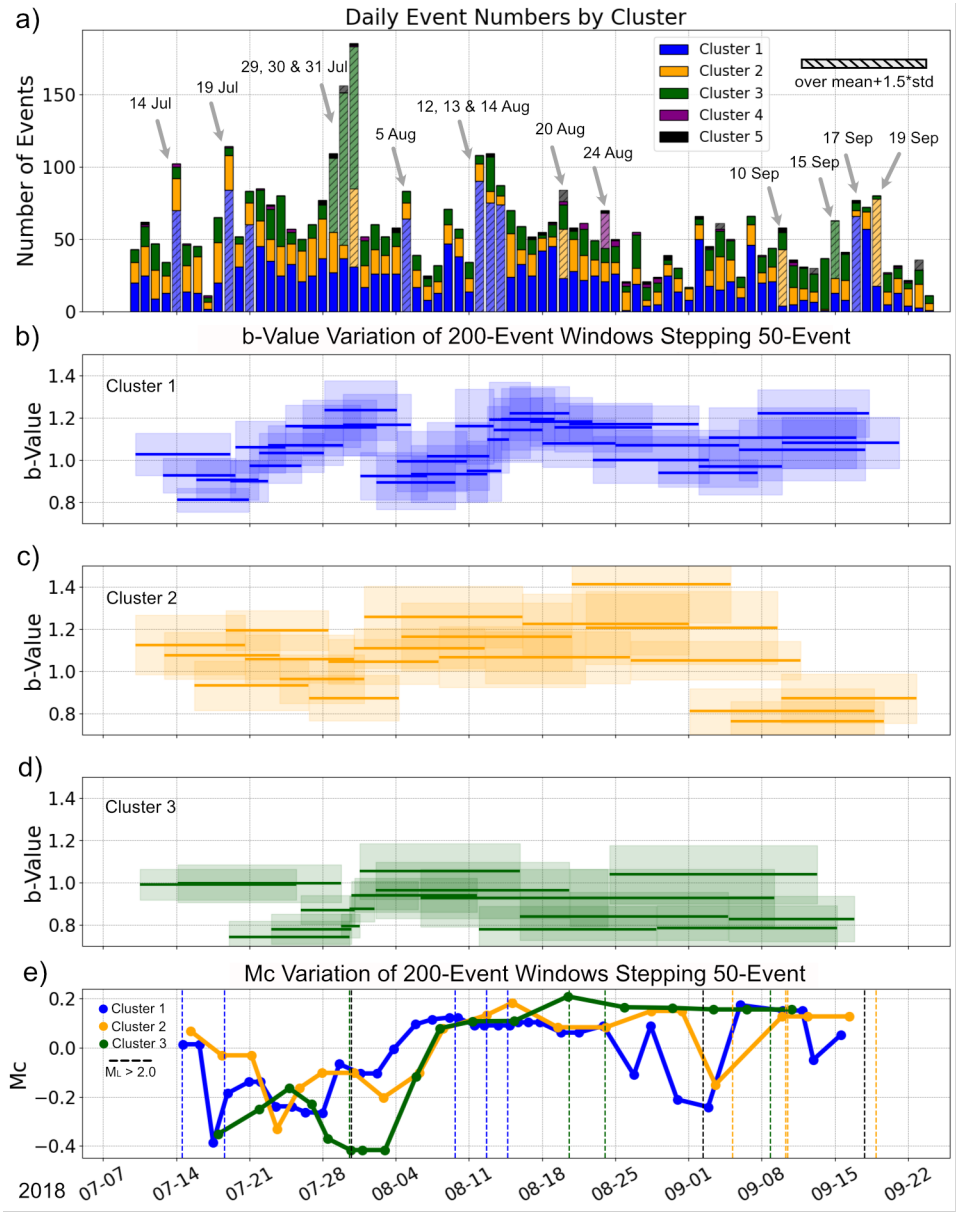

Figure 5 a) Histogram of daily relocated events for each cluster. Hatched bars indicate days where event counts exceed the cluster mean by 1.5 standard deviations (top 6.68%; see Supplemental Table S3). Arrows and labels mark these dates. b–d) b-values calculated using the maximum likelihood method (Aki, 1965) (see Equation 1) for sliding windows of 200 events with a step of 50 events across clusters 1, 2, and 3. Shaded areas represent uncertainties estimated from 1000 bootstrap iterations. (e) Variation of M_c across sliding windows, with data points plotted at the midpoints of each time window. Color dashed lines denote occurrence times of events with magnitude $M_L > 2.0$ in each cluster. Black dashed lines represent events with magnitude $M_L > 2.0$ not relocated by HypoDD.

reflecting an extended aftershock sequence and higher M_c. Similarly, the 30 July $M_L = 3.34$ mainshock and its afterschoks in Cluster 3 resulted in its b-value increase from ∼0.8 to ∼1.1 and M_c from -0.4 to -0.2 (Fig. 5a, d and e).

Between ∼21 July and 24 August (when another $M_L = 2.91$ occurred in Cluster 3), b-values for Clusters 1 and 3 seemed to exhibit an anti-correlated trend. This pattern corresponds to the anti-correlation in daily event counts highlighted in Supplemental Table S4 and Figure S17, suggesting potential seismicity migration between Clusters 1 and 3.

For Cluster 2 (Fig. 5c), the b-values remained predominantly around 1.2, except close to 30 July 2018 (an M_L 3.34 event in Cluster 3) and mid-September 2018. Around mid-September (Fig. 5e) which is marked by several large magnitude events ($M_L > 2.0$), a higher number of relocated events are distributed across different clusters (see Fig. 5a). However, the b-values dropped to approximately 0.8 for both Cluster 2 and Cluster 3. Given that we only have 3 months long datasets, it is not possible to make predictions on how the b-values will evolve after September 2018.

4.2 Focal Mechanism Solutions

We obtained a total of 17 focal mechanism solutions (FMS) that included all events with $M_L \geq 2.0$, which are all within clusters 1, 2, and 3 (see the complete list

in the Supplemental Materials, Table S2). The three largest earthquakes during the 2018 temporary deployment, M_w 3.55 on 30 July 2018, M_w 3.41 on 12 August 2018 and M_w 3.29 on 24 August 2018 (Fig. 4a) exhibited NW-striking normal fault plane solutions, with the 12 August 2018 event having a minor oblique component.

The NW-striking nodal planes of the 17 events dip steeply northeast or shallowly southwest (Fig. 4d plotted with Allmendinger et al. (2011)). Clusters 1–4 projected along the BB' cross-section profile define a steeply northeast dipping zone (Fig. 4c). The rake in the NE-dipping nodal planes is consistent with predominantly NE-vergent normal motion (Fig. 4d). Therefore, we interpret that the NE-dipping nodal planes define the orientation of the primary fault zone.

4.3 Surface deformation from Interferometric Synthetic Aperture Radar (InSAR)

We generated 12 day ascending coseismic interferograms (20 May to 1 June) for the 24 May 2018 M_w 5.0 earthquake, one for each orbit that covered the location of the earthquake (orbit numbers 29 and 131). There were very small potential surface deformation signals from the coseismic interferograms for this event (see the example in the Supplemental Figures S18 and S19). In order to remove atmospheric noise from the signal, we constructed a time series for the same event, using SBAS. The resulting annual velocity map (the total displacement over the time series converted to an annual velocity; Fig. 6a), shows a subtle signal east of the settlement of Anker. This comprises an ellipsoidal region of displacement towards the satellite on the western side (blue; ~40 mm/yr) and a smaller region of displacement away from the satellite on the east (red; ~20 mm/yr), co-located with the relocated seismicity (Fig. 3a) from July to September of that year.

The coseismic interferograms (29 March–10 April) for the 4 April 2021 M_w 5.4 earthquake may show a small tectonic signal, an oval fringe pattern south of the settlement of Anker, although there is significant atmospheric noise that may produce fringe patterns of a similar scale. However, the time-series velocity map for the 2021 M_w 5.4 event (Fig. 6b) shows a clear signal 11 km to the west of the United States Geological Survey (USGS) epicenter, defined by a lobe of displacement towards the satellite (blue, ~80 mm/yr) to the western side, with another region of deformation with the opposite sense of motion (red, ~300 mm/year) to the east. The events ($\geq M_c$ -0.22) recorded during the temporary seismic deployment in 2018 are plotted on top of the velocity map (Fig. 6), these events are within the area of maximum velocity away from the satellite.

Since only ascending track images were available for this region, we were unable to model the causative faulting associated with this event. However, we can make some observations about the fault(s) responsible, particularly since the tectonic signals for the 2018 and 2021 earthquakes had surface deformation in the same area (Fig. 6). In seismic interferograms, the surface projection of a fault is located between the deformation lobes, and as such we are able to infer the orientation of a fault responsible for the 4 April 2021 M_w 5.4 event. Our inferred fault (dashed line in Fig. 6b) strikes NNW–SSE (336°) and is approximately 9 km long. Relocated events from the temporary deployment plot in June–September 2018 within the eastern lobe of deformation, near the highest velocities away from the satellite. Our interpretation is that the fault responsible for the 4 April 2021 M_w 5.4 earthquake is dipping towards the east–northeast. This is consistent with the ENE-dipping nodal plane of the USGS focal mechanism (Fig. 6b). As the velocity gradient between the deformation lobes is smooth (Fig. 6b), without steps, it is likely that there was no surface rupture associated with the 4 April 2021 M_w 5.4 earthquake. However, the event would need to have been relatively shallow in order to observe ground deformation from an earthquake of this magnitude. This is in agreement with the body wave USGS moment tensor, which has a depth of 5 km. The 11 km difference between the USGS location and the InSAR deformation signal is not a concern, as seismic locations can have large uncertainties, especially in poorly instrumented regions (Xu et al., 2015). It is fairly common for seismic locations to be mislocated with respect to InSAR deformation (Weston et al., 2012). The surface deformation location is consistent with the upward projection from the tabular zone of the NW-striking, ENE-dipping earthquake clusters (compare Figures 4b, S16, and 6b).

5 Discussion

5.1 Events Distribution and Tectonic Context

In agreement with Sitali et al. (2022), our classification of the Kamanjab earthquake sequence as a 'swarm' is supported by the absence of a distinct mainshock–aftershock pattern (Fig. 3b) and the overall b-value of 1.277, as well as the Omori decay law. Although an enhanced catalog is not available for the immediate aftershock period of the M_w 5 earthquake on 24 May 2018, we evaluated potential decay rates from 10 July 2018 onward under different assumptions. Specifically, if there were k = 5000, 2000, or 1000 events on the first day after the mainshock, the resulting decay rates p would be 0.85, 0.64, or 0.48, respectively (Fig. 3b). We lack direct evidence for the actual number of aftershocks following this magnitude 5 event in Namibia and larger southern Africa region; however, 5000 daily events would be exceptionally high (Saunders et al., 2013), suggesting that the real number is likely lower and therefore indicative of a low decay rate consistent with swarm-like behavior. Moreover, the low coefficient of determination (maximum R^2 of ~0.2) for the Omori's Law fits (Supplemental Figure S6) underscores the difficulty of modeling the observed sequence as an aftershock decay; swarm-like behavior would be a more consistent interpretation.

Despite the general expectation that earthquake swarms exhibit a b-value significantly higher than 1.0, especially in hydrothermal susceptible regions, where b-values often range from 1.5 to 2.0 (e.g., Farrell et al., 2009; Glazner and McNutt, 2021; El-Isa and Eaton, 2014), our calculated b-value does not clearly reflect this char-

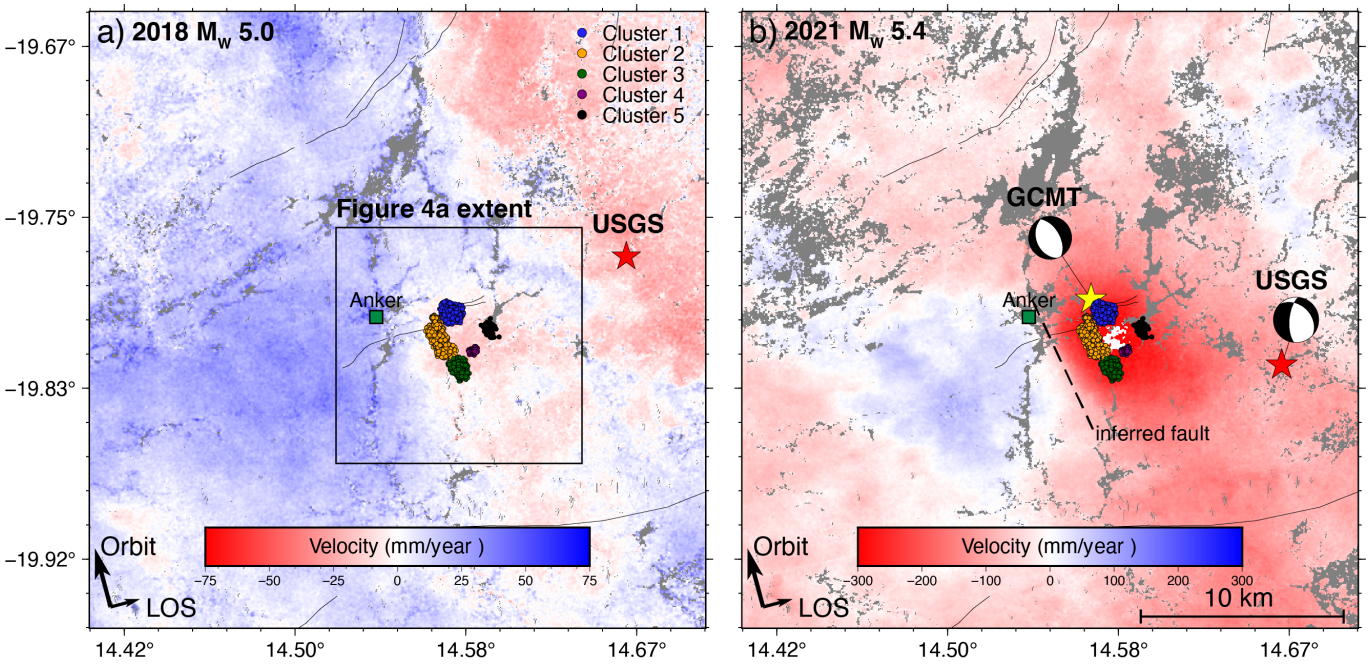

Figure 6 InSAR time series velocity maps for the 2018 and 2021 events. Arrows in the bottom left corner show the direction of the orbit and line-of-sight (LOS) of the satellite. Regional geologic faults and lineaments are solid black lines. Hillshade was made using SRTM data (Farr et al., 2007). a) Velocity map for the 5 month time series (May–September 2018) associated with the 24 May 2018 M_w 5.0 event (orbit #131). Red star is USGS epicenter for the M_w 5.0. Small circles are epicenters of relocated events with magnitudes over $M_c = -0.22$. Black rectangle shows the extent of Fig. 4a). b) Velocity map for the 6-month time series (March–August 2021) associated with the 4 April 2021 M_w 5.4 event (orbit #131). Note: the scale on the color bar used in b) is significantly larger than in a). USGS and GCMT focal mechanisms for the same event are also plotted. The dashed black line shows inflection between upthrown and downthrown blocks, corresponding to the inferred fault strike for the 4 April 2021 event, interpreted from the InSAR velocity maps.

acteristic swarm signature. One likely reason for this discrepancy is our strict phase association criterion, which requires at least four stations to record both P and S arrivals for an event to be included in our catalog, whereas only three of the temporary deployment stations are situated within 10 km of the 2018 seismicity (Fig. 3a and Supplemental Figure S10). For example, if we relax the detection threshold (e.g., reducing the minimum number of stations that record both P and S phases to three or even two but still keeping a total of eight phase picks), this will enable us to capture additional lower-magnitude events and hence increase the b-value in our catalog, providing stronger evidence of swarm-like behavior. However, relaxing the event detection criterion also comes with the risk of increased false detection rates.

We observed a nearly constant rate of approximately 100 events ($\geq M_c$) per day (Fig. 3b), with no significant variations in magnitude or frequency before and after largest M_w 3.55 (M_L 3.34) event, consistent with typical earthquake swarm behavior (Sykes, 1970). For the relocated events, the primary cluster, Cluster 1, exhibits relatively stable yet higher b-values (Fig. 5b) during periods without $M_L > 2.0$ events, further indicating swarm-type characteristics. Although our analysis covers only July–September 2018, it meets key criteria for classifying a swarm, including subsequent larger magnitude events (Mogi, 1963) and spatial migration of seismicity (Vidale and Shearer, 2006).

Several felt and damaging earthquakes occurred near the Anker settlement in the past decade, including an M_w 4.8 on 14 March 2018, an M_w 5.0 on 24 May 2018, an M_w 4.8 on 25 May 2018 and an M_w 5.4 on 4 April 2021 (U.S. Geological Survey, 2024). The continuity of seismic stations since 2009 indicates that an increase in recorded seismic activity after 2009 (Fig. 2c) reflects a genuine increase in seismic activity rather than a detection artifact.

Paleoseismic studies have shown that earthquakes up to M_w 7 likely occurred on NNW- to N-trending Pleistocene (Salomon et al., 2022; Muir et al., 2023) to recent (Korn and Martin, 1950; Korn, 1951; Klein, 1980) faults scarps 100s km to the south (Fig. 2a), but similarly oriented to the source fault of the Anker earthquakes as revealed by our FMS (Fig. 4) and InSAR maps (Fig. 6). The nearest recent seismicity has been linked to offshore active faults and presumed active magmatic systems in the Walvis Bay Ridge (Haxel and Dziak, 2005). However, given the great distances and lack of structural connectivity (Fig. 1), it is not likely that offshore seismicity is related to the Anker earthquake swarms.

5.2 Delineating the Anker Fault: InSAR Insights and Seismic Correlations

Analysis of InSAR data for 2018 and 2021 reveals surface deformation closely associated with seismic activity, allowing us to delineate the Anker fault with a NNW–SSE strike and an estimated rupture length of approximately 9 km (Fig. 6b). The normal shear sense indicated by

the FMS and the surface deformation pattern observed during the 4 April 2021 M_w 5.4 event suggest that the fault dips towards the NE, to intersect the earthquake clusters at depth. The USGS focal mechanism and the principal extension directions of the events M_w 3.55 on 30 July 2018, M_w 3.41 on 12 August 2018 and M_w 3.29 on 24 August 2018 are also consistent with normal faulting with NNW strike and ENE dip (Fig. 4a, d, and Fig. 6b).

InSAR has been shown to enhance the location of moderately-sized earthquakes and assist in active fault identification. In areas with limited seismic instrumentation, earthquake mislocations can pose challenges in correlating InSAR-detected deformations with seismic epicenters. Studies by Weston et al. (2012); Xu et al. (2015), among others, have shown that InSAR can produce more accurate fault locations compared to epicentral locations in the global catalog if there is insufficient station coverage close to earthquake source. Due to the sparse seismic network in the area at the time of the earthquake occurrence, we interpret the ∼10 km offset of the USGS epicenter of the M_w 5.4 on 4 April 2021 from the InSAR deformation mapped Anker fault and the associated seismic swarm to likely reflect the USGS epicenter location error (∼7 km, United States Geological Survey, 2021). Furthermore, the Global Centroid Moment Tensor (GCMT) location (Dziewonski et al., 1981; Ekström et al., 2012) for M_w 5.4 on 4 April 2021 is located nearly on the fault line interpreted from the InSAR deformation in Fig. 6b.

Our analyses confirm that the locations of earthquake swarms detected during the July to September 2018 temporary seismic network deployment are co-located with the surface deformation linked to the M_w 5.0 event in May 2018 and the M_w 5.4 event in April 2021. The seismic activity and associated surface deformation suggest the existence of a NNW–SSE striking and NE-dipping fault zone that we call the Anker fault zone, which produces normal to normal oblique-slip earthquakes. This fault orientation is consistent with activation in the horizontal maximum regional stress direction for normal faulting (Heidbach et al., 2016, 2018). The spatial distribution of relocated events, while not delineating a single linear fault structure, suggests the presence of a complex fault zone several kilometers wide, with seismogenesis occurring at shallow depths (∼2–7 km).

5.3 Potential Swarm Trigger Mechanism

The absence of anthropogenic triggers within a radius of ∼150 km of the Anker fault is confirmed by the Geological Survey database and Namibia's annual mine reports (Chamber of Mines Namibia Annual Reports). This finding implies that the observed swarms are naturally driven. We hypothesize that a key mechanism causing this seismicity could be variations in pore pressure within the Anker fault zone, potentially influenced by hydrothermal fluid flow.

Groundwater circulation in hot spring systems can alter the pore pressure, which if channeled through fluid conduits to a pre-existing fault can in turn facilitate fault slip and modulate seismic activity. Previous studies have established links between the occurrence of earthquakes and hydrothermal systems, where changes in the pore pressure of thermal fluid flow play a key role (e.g. Cox et al., 2012; Yan et al., 2020; Yamanaka and Adachi, 2024). Evidence of several hot springs in the region, including at least one permanent thermal hot spring near the study area (Fig. 3a), supports the possibility of ongoing hydrothermal activity influencing seismic clusters (Sracek et al., 2015; Soetaert et al., 2022). These hot springs provide a plausible mechanism for the observed spatial and temporal changes in seismicity, highlighting the possible role of hydrothermal systems in modulating earthquake patterns in the Kamanjab area.

Fluctuations in surface deformation and fluid pressure may also be influenced by tidal forces (Yunjun et al., 2022). To search for tidal signatures, we performed a Fast Fourier Transform (FFT) analysis on both the initial ML catalog and the relocated catalog, using daily time series of event counts, maximum and minimum magnitudes respectively (Supplemental Figures S20 and S21). While both catalogs show spectral peaks in the maximum-magnitude series that exceed the 95% confidence level, the event-count and minimum-magnitude series display multiple peaks at periods shorter than 13.6 days, but there is no significant peak at 6, 12, or 18 hours which would indicate tidal forcing. This indicates that complex triggering mechanisms may operate on multiple time scales (days to weeks). Although we do not rule out the role of tidal forcing, the absence of a characteristic timescale match suggests that it may not be the sole controlling factor. Furthermore, appropriate declustering for a seismicity catalog covering a longer time period is required before attribution of tidal modulations (Hirose et al., 2024).

The occurrence of earthquakes in the Anker settlement and surrounding areas prior to 2018 indicates that seismic triggering has been an ongoing process over time (Fig. 2). Only the damaging earthquakes that began in 2018 were significant enough to motivate additional seismic station deployments. The structural damage that motivated the densification of the monitoring stations during 2018 could occur when seismic triggering reached a critical threshold due, for example, to continued loading from the hydrothermal activity. Therefore, we strongly advocate for long-term, permanent seismic station coverage, including data telemetry and efficient sharing, for near real-time monitoring and better understanding of the earthquake triggering mechanisms in the Kamanjab Inlier.

6 Conclusion

We have advanced the identification of active earthquake swarms in the Kamanjab area of NW Namibia through a synergistic approach that combines seismological data analysis and studies of the mechanism of the earthquake source. Using machine learning in conjunction with relocation algorithms, we have refined the locations of approximately 4500 events with horizontal and vertical relative location uncertainty, averaging ∼50 and ∼65 meters, respectively, recorded during the tem-

porary station deployment near the Anker settlement from July to September 2018. The event locations align with the InSAR signals of the M_w 5.4 event that occurred on 4 April 2021, marking the first-time identification of the "Anker fault". The focal mechanism solutions of $M_L \geq 2.0$ earthquakes are consistent with a NNW–SSE striking, steeply NE-dipping fault zone comprising multiple fault planes compatible with the InSAR surface deformation and the USGS focal mechanism solution of the M_w 5.4 earthquake. Nearby hot springs corroborate our suggestion of deep-seated fluid migration that could provide the necessary conditions to trigger this earthquake swarm. Seismicity in the Kamanjab region has caused damage to infrastructure and negatively affected the livelihoods of the Anker community, but it provides a unique natural setting for interrogating intraplate earthquake sources. Expanding seismological observation capacity in this area will allow long-term monitoring of earthquake recurrence, migration patterns, and triggering mechanisms, and can contribute to building the local seismology capacity needed to mitigate future seismic hazards.

Acknowledgements

The study was supported by the McGill University Graduate (Virtual) Mobility Grant, 2020. Christie Rowe and Moses Angombe were supported by a National Science and Engineering Research Council of Canada (NSERC) Discovery Grant RGPIN-2022-04192. Justin Chien and Yajing Liu are supported by NSERC Discovery Grant RGPIN-2024-05737. The authors thank the Geological Survey of Namibia, Ministry of Mines and Energy Namibia, for providing seismology, geological data products, and in-kind contributions. This paper benefited from discussions with Drs. Rebecca M. Harrington, Alessandro Verdecchia, John Onweumeka, Andres Peña-Castro, and team members of the Earthquake Processes Group (EQP) at McGill University. In addition, we appreciate Dr. Fanny Soetaert for insightful discussions and data on Namibian hot springs. We thank Ester Kapuka (Oshiwambo), Michelle Hailonga, Charlotte Mbinda, Victorine Koujo (Otjiherero), Dixon Bernardu, Wycliffe !Haoseb, Augustinus /Ochurub, Manfred Goreseb, Sydney Garoeb, Lydia Dreyer (Khoekhoegowab), Cornelia Gous (Afrikaans) and Ute Schreiber, Tobias Stephan (German) for their contributions to translating the abstract into multiple languages. This paper benefited greatly from the contributions and constructive feedback of Victoria Stevens, two anonymous reviewers, and editor Matt Ikari.

Data and code availability

All the supplemental materials and the complete event catalog for this study can be downloaded from https://doi.org/10.5683/SP3/DUPW6Q. Source parameters (epicenters and focal mechanism solutions) for the M_w 5.4 on 4 May 2021 were obtained from USGS (https://earthquake.usgs.gov/earthquakes/search/) and GCMT (https://www.globalcmt.org/CMTsearch.html). Sentinel 1 data can be downloaded from https://browser.dataspace.copernicus.eu. The analysis packages are open source and freely available. This includes PYGMT, ObsPy, NonLinLoc (Lomax et al., 2014), HypoDD, GMT (Wessel et al., 2019), and GMTSAR (Sandwell et al., 2011).

Competing interests

The authors have no competing interests to declare.

References

Aki, K. Maximum likelihood estimate of b in the formula log N= a-bM and its confidence limits. *Bull. Earthquake Res. Inst., Tokyo Univ.*, 43:237–239, 1965.

Allmendinger, R. W., Cardozo, N., and Fisher, D. M. *Structural geology algorithms: Vectors and tensors*. Cambridge University Press, 2011.

Andreoli, M., Doucouré, M., Van Bever Donker, J., Brandt, D., and Andersen, N. Neotectonics of southern Africa – a review. In *Africa Geoscience Review*. 3(1):1–16, 1996. OCLC Number/Unique Identifier: 5866438012.

Becker, T., Schreiber, U., Kampunzu, A. B., and Armstrong, R. Mesoproterozoic rocks of Namibia and their plate tectonic setting. *Journal of African Earth Sciences*, 46(1-2):112–140, 2006. doi: 10.1016/j.jafrearsci.2006.01.015.

Berardino, P., Fornaro, G., Lanari, R., and Sansosti, E. A new algorithm for surface deformation monitoring based on small baseline differential SAR interferograms. *IEEE Transactions on geoscience and remote sensing*, 40(11):2375–2383, 2002. doi: 10.1109/TGRS.2002.803792.

Chamber of Mines Namibia Annual Reports, 2016–2021. Retrieved Dec 2023 from https://chamberofmines.org.na/annual-reviews/.

Chamberlain, C. J., Hopp, C. J., Boese, C. M., Warren-Smith, E., Chambers, D., Chu, S. X., Michailos, K., and Townend, J. EQcorrscan: Repeating and near-repeating earthquake detection and analysis in Python. *Seismological Research Letters*, 89(1): 173–181, 2018. doi: 10.1785/0220170151.

Clemson, J., Cartwright, J., and Booth, J. Structural segmentation and the influence of basement structure on the Namibian passive margin. *Journal of the Geological Society*, 154(3):477–482, 1997. doi: 10.1144/gsjgs.154.3.0477.

Corner, B. and Durrheim, R. J. An integrated geophysical and geological interpretation of the southern African lithosphere. In *Geology of southwest Gondwana*, pages 19–61. Springer, 2018. doi: 10.1007/978-3-319-68920-3_2.

Coward, M. The junction between Pan African mobile belts in Namibia: Its structural history. *Tectonophysics*, 76(1-2):59–73, 1981. doi: 10.1016/0040-1951(81)90253-5.

Cox, S. C., Menzies, C. D., Sutherland, R., Denys, P. H., Chamberlain, C., and Teagle, D. A. Changes in hot spring temperature and hydrogeology of the Alpine Fault hanging wall, New Zealand, induced by distal South Island earthquakes. *Crustal Permeability*, pages 228–248, 2012. doi: 10.1002/9781119166573.ch19.

Dziewonski, A. M., Chou, T.-A., and Woodhouse, J. H. Determination of earthquake source parameters from waveform data for studies of global and regional seismicity. *Journal of Geophysical Research: Solid Earth*, 86(B4):2825–2852, 1981. doi: 10.1029/JB086iB04p02825.

Ekström, G., Nettles, M., and Dziewoński, A. The global CMT project 2004–2010: Centroid-moment tensors for 13,017 earthquakes.

Physics of the Earth and Planetary Interiors, 200:1–9, 2012. doi: 10.1016/j.pepi.2012.04.002.

El-Isa, Z. H. and Eaton, D. W. Spatiotemporal variations in the b-value of earthquake magnitude–frequency distributions: Classification and causes. *Tectonophysics*, 615:1–11, 2014. doi: 10.1016/j.tecto.2013.12.001.

ESA. Sentinel-1 Acquisition Plans, 2024. Available online: https://sentinels.copernicus.eu/web/sentinel/copernicus/sentinel-1/acquisition-plans.

Ester, M., Kriegel, H.-P., Sander, J., and Xu, X. Density-based spatial clustering of applications with noise. In *Int. Conf. knowledge discovery and data mining*, volume 240, 1996.

Farr, T. G., Rosen, P. A., Caro, E., Crippen, R., Duren, R., Hensley, S., Kobrick, M., Paller, M., Rodriguez, E., Roth, L., et al. The shuttle radar topography mission. *Reviews of geophysics*, 45(2), 2007. doi: 10.1029/2005RG000183.

Farrell, J., Husen, S., and Smith, R. B. Earthquake swarm and b-value characterization of the Yellowstone volcano-tectonic system. *Journal of Volcanology and Geothermal Research*, 188(1-3): 260–276, 2009. doi: 10.1016/j.jvolgeores.2009.08.008.

Foulger, G. R., Wilson, M. P., Gluyas, J. G., Julian, B. R., and Davies, R. J. Global review of human-induced earthquakes. *Earth-Science Reviews*, 178:438–514, 2018. doi: 10.1016/j.earscirev.2017.07.008.

Frechet, J. *Sismogenese et doublets sismiques*. PhD thesis, Universite Scientifique et Medicale de Grenoble, 1985.

Geological Survey of Namibia. SHEET 1914 - KAMANJAB, 2009. Geological mapping by H. Porada (1970), R. Hedberg (1975), CDM Mineral Services (1979-80), T. Becker (2005), E. Muvangua, K. Mhopjeni & A. Muyongo (2008), P.F. Hoffman & G.P. Halverson (2008). Map and legend compiled by U.M. Schreiber. Cartographic planning by D.L. Richards & U.M. Schreiber. Digital cartography by D. Hiskia, S. Cloete & U.M. Schreiber. Released on Open File by the Geological Survey of Namibia.

Geological Survey of Namibia Earthquake catalog 1910 to 2020, 2021. Available on request: Department of Geological Survey of Namibia, Ministry of Mines and Energy, 6 Aviation Road, Windhoek, Namibia, https://www.mme.gov.na.

Geological Survey of Namibia Online Database. Earth Data Namibia, Geological and Mineral Information System. https://www.mme.gov.na/edn, 2024. Accessed February 23 2024.

Glazner, A. F. and McNutt, S. R. Relationship Between Dike Injection and b-Value for Volcanic Earthquake Swarms. *Journal of Geophysical Research: Solid Earth*, 126(12):e2020JB021631, 2021. doi: 10.1029/2020JB021631.

Harris, F. J. On the use of windows for harmonic analysis with the discrete Fourier transform. *Proceedings of the IEEE*, 66(1):51–83, 1978. doi: 10.1109/PROC.1978.10837.

Hartman, A. Kunene school to be relocated due to tremors. *The Namibian*, 24 May, 2018. https://www.namibian.com.na/177711/archive-read/Kunene-school-to-be-relocated-due-to-tremors.

Haxel, J. and Dziak, R. Evidence of explosive seafloor volcanic activity from the Walvis Ridge, South Atlantic Ocean. *Geophysical Research Letters*, 32(13), 2005. doi: 10.1029/2005GL023205.

Heidbach, O., Rajabi, M., Reiter, K., Ziegler, M., and WSM Team. World Stress Map Database Release V. 1.1. Technical report, GFZ Data Services, 2016. doi: 10.5880/WSM.2016.001.

Heidbach, O., Rajabi, M., Cui, X., Fuchs, K., Müller, B., Reinecker, J., Reiterg, K., Tingay, M., Wenzel, F., Xie, F., Ziegler, M. O., Zoback, M.-L., and Zoback, M. The World Stress Map database release 2016: Crustal stress pattern across scales. *Tectonophysics*, 744: 484–498, 2018. doi: 10.1016/j.tecto.2018.07.007.

Heimann, S., Isken, M., Kühn, D., Sudhaus, H., Steinberg, A., Daout, S., Cesca, S., Bathke, H., and Dahm, T. Grond: A probabilistic earthquake source inversion framework. Technical report, GFZ Data Services, 2018. doi: 10.5880/GFZ.2.1.2018.003.

Heimann, S., Vasyura-Bathke, H., Sudhaus, H., Isken, M. P., Kriegerowski, M., Steinberg, A., and Dahm, T. A Python framework for efficient use of pre-computed Green's functions in seismological and other physical forward and inverse source problems. *Solid Earth*, 10(6):1921–1935, 2019. doi: 10.5194/se-10-1921-2019.

Hirose, F., Tamaribuchi, K., Kobayashi, A., and Maeda, K. Relation between earthquake swarm activity and tides in the Noto region, Japan. *Earth, Planets and Space*, 76(1):37, 2024. doi: 10.1186/s40623-024-01985-x.

Hutchins, D. and Wackerle, R. The high resolution airborne geophysical survey programme of Namibia: a success story in promoting mineral exploration. In *Proceedings of exploration*, volume 7, pages 879–883, 2007. https://911metallurgist.com/blog/wp-content/uploads/2015/10/The-High-Resolution-Airborne-Geophysical-Survey-Programme-of-Namibia.pdf.

International Seismological Center, 2000–2021. Retrieved Jan 2023 from http://www.isc.ac.uk/registries/search/.

Iwata, D. and Nanjo, K. Z. Adaptive estimation of the Gutenberg–Richter b value using a state space model and particle filtering. *Scientific Reports*, 14(1):4630, 2024. doi: 10.1038/s41598-024-54576-x.

Jelsma, H. A., McCourt, S., Perritt, S. H., and Armstrong, R. A. The Geology and Evolution of the Angolan Shield, Congo Craton. In Siegesmund, S., Basei, M. A. S., Oyhantçabal, P., and Oriolo, S., editors, *Geology of Southwest Gondwana*, pages 217–239. Springer International Publishing, Cham, 2018. doi: 10.1007/978-3-319-68920-3$_9$.

Jenatton, L., Guiguet, R., Thouvenot, F., and Daix, N. The 16,000-event 2003–2004 earthquake swarm in Ubaye (French Alps). *Journal of Geophysical Research: Solid Earth*, 112(B11), 2007. doi: 10.1029/2006JB004878.

Kadiri, A., Sitali, M., and Midzi, V. Probabilistic seismic hazard assessment in Namibia. *Journal of African Earth Sciences*, 202: 104933, 2023. doi: 10.1016/j.jafrearsci.2023.104933.

Kirkpatrick, L. H. and Green, A. N. Antecedent geologic control on nearshore morphological development: The wave dominated, high sediment supply shoreface of southern Namibia. *Marine Geology*, 403:34–47, 2018. doi: 10.1016/j.margeo.2018.05.003.

Kissling, E., Ellsworth, W., Eberhart-Phillips, D., and Kradolfer, U. Initial reference models in local earthquake tomography. *Journal of Geophysical Research: Solid Earth*, 99(B10):19635–19646, 1994. doi: 10.1029/93JB03138.

Klein, J. Pleistocene to Recent faulting in the area west of Omaruru (SWA/Namibia). *Reg. Geol. Ser. Open File Rep. RG*, 4:28, 1980.

Konopásek, J., Kröner, S., Kitt, S. L., Passchier, C. W., and Kröner, A. Oblique collision and evolution of large-scale transcurrent shear zones in the Kaoko belt, NW Namibia. *Precambrian Research*, 136(2):139–157, 2005. doi: 10.1016/j.precamres.2004.10.005.

Korn, H. and Martin, H. Erdbeben in Südwestafrika. *Geologische Rundschau*, 38(1):19–23, 1950. doi: 10.1007/BF01766569.

Korn, H. & Martin, H. The seismicity of South-West Africa. *South African Journal of Geology*, 54(1):85–88, 1951. doi: 10.1016/S0040-1951(02)00047-1.

Kühn, D., Heimann, S., Isken, M. P., Ruigrok, E., and Dost, B. Probabilistic moment tensor inversion for hydrocarbon-induced seismicity in the Groningen gas field, The Netherlands, Part 1: Testing. *Bulletin of the Seismological Society of America*, 110(5):

2095–2111, 2020. doi: 10.1785/0120200099.

Lehmann, J., Saalmann, K., Naydenov, K. V., Milani, L., Belyanin, G. A., Zwingmann, H., Charlesworth, G., and Kinnaird, J. A. Structural and geochronological constraints on the Pan-African tectonic evolution of the northern Damara Belt, Namibia. *Tectonics*, 35(1):103–135, 2016. doi: 10.1002/2015TC003899.

Li, S., Xu, W., and Li, Z. Review of the SBAS InSAR Time-series algorithms, applications, and challenges. *Advances in InSAR algorithms, deformation monitoring and source parameter inversion*, 13(2):114–126, 2022. doi: 10.1016/j.geog.2021.09.007.

Lomax, A., Michelini, A., and Curtis, A. Earthquake Location, Direct, Global-Search Methods. In Meyers, R., editor, *Encyclopedia of Complexity and Systems Science*, volume 5, pages 2449–2473. Springer New York, New York, 2014. doi: 10.1007/978-3-642-27737-5_150-2.

López-Comino, J. Á., Braun, T., Dahm, T., Cesca, S., and Danesi, S. On the source parameters and genesis of the 2017, Mw 4 Montesano earthquake in the outer border of the Val d'Agri Oilfield (Italy). *Frontiers in Earth Science*, 8:617794, 2021. doi: 10.3389/feart.2020.617794.

MacQueen, J. Some methods for classification and analysis of multivariate observations. In *Proceedings of the fifth Berkeley symposium on mathematical statistics and probability*, volume 1/14, pages 281–297, 1967.

Mangongolo, A., Hutchins, D., and Miller, R. Seismicity of Namibia from 1910 to 2006. *Geology of Namibia*, pages 1–27, 2008.

Martin, H. and Porada, H. The intracratonic branch of the Damara orogen in South West Africa I. Discussion of geodynamic models. *Precambrian Research*, 5(4):311–338, 1977. doi: 10.1016/0301-9268(77)90039-0.

Midzi, V., Saunders, I., Brandt, M. B., and Molea, T. 1-D velocity model for use by the SANSN in earthquake location. *Seismological Research Letters*, 81(3):460–466, 2010. doi: 10.1785/gssrl.81.3.460.

Midzi, V., Bommer, J., Strasser, F., Albini, P., Zulu, B., Prasad, K., and Flint, N. An intensity database for earthquakes in South Africa from 1912 to 2011. *Journal of Seismology*, 17:1183–1205, 2013. doi: 10.1007/s10950-013-9387-y.

Midzi, V., Manzunzu, B., Zulu, B. S., Mulabisana, T., Myendeki, S., and Mangongolo, A. Impact of recent moderately sized earthquakes in South Africa: Macroseismic investigations of the 18 November and 2 December 2013 earthquakes. *South African Journal of Geology*, 118(4):373–388, 2015. doi: 10.2113/gssajg.118.4.373.

Miller, R. M. The Pan-African Damara Orogen of South West Africa/-Namibia. In *Evolution of the Damara Orogen of South West Africa/Namibia*. Geological Society of South Africa, 1983. INIS RN 17021045.

Minetto, R., Helmstetter, A., Schwartz, S., Langlais, M., Nomade, J., and Guéguen, P. Analysis of the spatiotemporal evolution of the Maurienne swarm (French Alps) based on earthquake clustering. *Earth and Space Science*, 9(7):e2021EA002097, 2022. doi: 10.1029/2021EA002097.

Mogi, K. Some discussions on aftershocks, foreshocks and earthquake swarms-the fracture of a semi finite body caused by an inner stress origin and its relation to the earthquake phenomena. *Bull. Earthq. Res. Inst.*, 41:615–658, 1963.

Mousavi, S. M., Ellsworth, W. L., Zhu, W., Chuang, L. Y., and Beroza, G. C. Earthquake transformer—an attentive deep-learning model for simultaneous earthquake detection and phase picking. *Nature communications*, 11(1):1–12, 2020. doi: 10.1038/s41467-020-17591-w.

Muir, R., Whitehead, B., New, T., Stevens, V., Macey, P., Groenewald, C., Salomon, G., Kahle, B., Hollingsworth, J., and Sloan, R. Exceptional scarp preservation in SW Namibia reveals geological controls on large magnitude intraplate seismicity in southern Africa. *Tectonics*, 42(4):e2022TC007693, 2023. doi: 10.1029/2022TC007693.

Münchmeyer, J. PyOcto: A high-throughput seismic phase associator. *arXiv preprint arXiv:2310.11157*, 2023.

Namibian Broadcasting Corporation. Anker residents share earthquake experiences. https://www.youtube.com/watch?v=JljzlbISNxE, April 2021.

O'Connor, J. M. and Duncan, R. A. Evolution of the Walvis Ridge-Rio Grande Rise hot spot system: Implications for African and South American plate motions over plumes. *Journal of Geophysical Research: Solid Earth*, 95(B11):17475–17502, 1990a. doi: 10.1029/JB095iB11p17475.

O'Connor, J. M. and Duncan, R. A. Evolution of the Walvis Ridge-Rio Grande Rise hot spot system: Implications for African and South American plate motions over plumes. *Journal of Geophysical Research: Solid Earth*, 95(B11):17475–17502, 1990b. doi: 10.1029/JB095iB11p17475.

Omori, F. *On the after-shocks of earthquakes*. PhD thesis, The University of Tokyo, 1895. doi: 10.15083/00037562.

Parsons, T. Global Omori law decay of triggered earthquakes: Large aftershocks outside the classical aftershock zone. *Journal of Geophysical Research: Solid Earth*, 107(B9):ESE–9, 2002. doi: 10.1029/2001JB000646.

Passchier, C., Trouw, R., Ribeiro, A., and Paciullo, F. Tectonic evolution of the southern Kaoko belt, Namibia. *Journal of African Earth Sciences*, 35(1):61–75, 2002. doi: 10.1016/S0899-5362(02)00030-1.

Petersen, G. M., Cesca, S., Heimann, S., Niemz, P., Dahm, T., Kühn, D., Kummerow, J., and Plenefisch, T. Regional centroid moment tensor inversion of small to moderate earthquakes in the Alps using the dense AlpArray seismic network: Challenges and seismotectonic insights. *Solid Earth*, 12:1233–1257, 2021. doi: 10.5194/se-12-1233-2021.

Pickford, M. The geology of the Kamanjab Inlier, northern Namibia. *Memoir of the Geological Suvery of Namibia*, 23:1–136, 2023. doi: 10.1016/j.tecto.2009.03.006.

Porada, H. The damara-ribeira orogen of the Pan-Africanbrasiliano cycle in Namibia (Southwest Africa) and Brazil as interpreted in terms of continental collision. *Tectonophysics*, 57(2-4):237–265, 1979. doi: 10.1016/0040-1951(79)90150-1.

Porada, H., Ahrendt, H., Behr, H.-J., and Weber, K. The join of the coastal and intracontinental branches of the Damara Orogen, Namibia, South West Africa. In *Intracontinental fold belts*, pages 901–912. Springer, 1983. doi: 10.1007/978-3-642-69124-9$_4$0.

Prave, A. R. Tale of three cratons: Tectonostratigraphic anatomy of the Damara orogen in northwestern Namibia and the assembly of Gondwana. *Geology*, 24(12):1115–1118, 1996. doi: 10.1130/0091-7613(1996)024%3C1115:TOTCTA%3E2.3.CO;2.

Raab, M. J., Brown, R. W., Gallagher, K., Carter, A., and Weber, K. Late Cretaceous reactivation of major crustal shear zones in northern Namibia: constraints from apatite fission track analysis. *Tectonophysics*, 349(1-4):75–92, 2002. doi: 10.1016/S0040-1951(02)00047-1.

Rousseeuw, P. J. Silhouettes: a graphical aid to the interpretation and validation of cluster analysis. *Journal of computational and applied mathematics*, 20:53–65, 1987. doi: 10.1016/0377-0427(87)90125-7.

Salomon, G., New, T., Muir, R., Whitehead, B., Scheiber-Enslin, S., Smit, J., Stevens, V., Kahle, B., Kahle, R., Eckardt, F., et al. Geomorphological and geophysical analyses of the Hebron Fault,

SW Namibia: implications for stable continental region seismic hazard. *Geophysical Journal International*, 229(1):235–254, 2022. doi: 10.1093/gji/ggab466.

Sandwell, D., Mellors, R., Tong, X., Wei, M., and Wessel, P. GMTSAR: An InSAR processing system based on generic mapping tools. Technical report, UC San Diego: Scripps Institution of Oceanography, 2011. https://escholarship.org/uc/item/8zq2c02m.

Saunders, I., Ottemöller, L., Brandt, M. B., and Fourie, C. J. Calibration of an M_L scale for South Africa using tectonic earthquake data recorded by the South African National Seismograph Network: 2006 to 2009. *Journal of seismology*, 17:437–451, 2013. doi: 10.1007/s10950-012-9329-0.

Schmidt, D. A. and Bürgmann, R. Time-dependent land uplift and subsidence in the Santa Clara valley, California, from a large interferometric synthetic aperture radar data set. *Journal of Geophysical Research: Solid Earth*, 108(B9), 2003. doi: 10.1029/2002JB002267.

Shcherbakov, R., Turcotte, D. L., and Rundle, J. B. A generalized Omori's law for earthquake aftershock decay. *Geophysical research letters*, 31(11), 2004. doi: 10.1029/2004GL019808.

Sitali, M., Manzunzu, B., Midzi, V., Shipena, S., and Lushetile, B. Seismotectonic analysis of the Anker area, Kunene region northwestern Namibia. *Journal of Seismology*, pages 1–13, 2022. doi: 10.1007/s10950-022-10079-8.

Soetaert, F., Wanke, H., Dupuy, A., Lusuekikio, V., Gaucher, E. C., Bordmann, V., Fleury, J.-M., and Franceschi, M. Toward the sustainable use of groundwater springs: A case study from Namibia. *Sustainability*, 14(7):3995, 2022. doi: 10.3390/su14073995.

Sracek, O., Wanke, H., Ndakunda, N., Mihaljevič, M., and Buzek, F. Geochemistry and fluoride levels of geothermal springs in Namibia. *Journal of Geochemical Exploration*, 148:96–104, 2015. doi: 10.1016/j.gexplo.2014.08.012.

Swart, R. The sedimentology of the Zerrissene turbidite system, Damara Orogen, Namibia. *Commun. Geol. Surv. Namibia*, 13:57, 1992.

Sykes, L. R. Earthquake swarms and sea-floor spreading. *Journal of Geophysical Research*, 75(32):6598–6611, 1970.

Tong, X. and Schmidt, D. Active movement of the Cascade landslide complex in Washington from a coherence-based InSAR time series method. *Remote Sensing of Environment*, 186: 405–415, 2016. doi: 10.1016/j.rse.2016.09.008.

Trnkoczy, A. Understanding and parameter setting of STA/LTA trigger algorithm. In *New manual of seismological observatory practice (NMSOP)*, pages 1–20. Deutsches GeoForschungsZentrum GFZ, 2009. https://gfzpublic.gfz-potsdam.de/rest/items/item_4097/component/file_4098/content.

United States Geological Survey. M 5.4 - 68 km NNW of Khorixas, Namibia. Web interface; Latest Earthquakes database, USGS National Earthquake Information Center, 2021. doi: 10.1144/gsjgs.154.3.0477. Retrieved 21 February, 2024 from https://earthquake.usgs.gov/earthquakes/eventpage/us6000dyuk/origin/detail.

U.S. Geological Survey. Earthquake Lists, Maps, and Statistics, 2024. https://www.usgs.gov/natural-hazards/earthquake-hazards/lists-maps-and-statistics. Accessed: 2024-10-01.

Vidale, J. E. and Shearer, P. M. A survey of 71 earthquake bursts across southern California: Exploring the role of pore fluid pressure fluctuations and aseismic slip as drivers. *Journal of Geophysical Research: Solid Earth*, 111(B5), 2006. doi: 10.1029/2005JB004034.

Viola, G., Andreoli, M., Ben-Avraham, Z., Stengel, I., and Reshef, M. Offshore mud volcanoes and onland faulting in southwestern Africa: neotectonic implications and constraints on the regional stress field. *Earth and Planetary Science Letters*, 231(1-2): 147–160, 2005. doi: 10.1016/j.epsl.2004.12.001.

Waldhauser, F. and Ellsworth, W. L. A double-difference earthquake location algorithm: Method and application to the northern Hayward fault, California. *Bulletin of the seismological society of America*, 90(6):1353–1368, 2000. doi: 10.1785/0120000006.

Wang, R. A simple orthonormalization method for stable and efficient computation of Green's functions. *Bulletin of the Seismological Society of America*, 89(3):733–741, 1999. doi: 10.1785/BSSA0890030733.

Wessel, P., Luis, J. F., Uieda, L., Scharroo, R., Wobbe, F., Smith, W. H. F., and Tian, D. The Generic Mapping Tools Version 6. *Geochemistry, Geophysics, Geosystems*, 20(11):5556–5564, 2019. doi: 10.1029/2019GC008515.

Weston, J., Ferreira, A. M., and Funning, G. J. Systematic comparisons of earthquake source models determined using InSAR and seismic data. *Tectonophysics*, 532:61–81, 2012. doi: 10.1016/j.tecto.2012.02.001.

White, S., Stollhofen, H., Stanistreet, I. G., and Lorenz, V. Pleistocene to recent rejuvenation of the Hebron Fault, SW Namibia. *Geological Society, London, Special Publications*, 316 (1):293–317, 2009. doi: 10.1144/SP316.18.

Xavier, C. and Reporter, S. Anker school receives earthquake hostel blocks. *New Era Newspaper*, 19 May, 2022. https://neweralive.na/os/posts/anker-school-receives-earthquake-hostel-blocks.

Xiao, Z., Wang, J., Liu, C., Li, J., Zhao, L., and Yao, Z. Siamese earthquake transformer: A pair-input deep-learning model for earthquake detection and phase picking on a seismic array. *Journal of Geophysical Research: Solid Earth*, 126(5):e2020JB021444, 2021. doi: 10.1029/2020JB021444.

Xu, W., Dutta, R., and Jónsson, S. Identifying active faults by improving earthquake locations with InSAR data and Bayesian estimation: the 2004 Tabuk (Saudi Arabia) earthquake sequence. *Bulletin of the Seismological Society of America*, 105 (2A):765–775, 2015. doi: 10.1785/0120140289.

Xu, X., Sandwell, D. T., Tymofyeyeva, E., González-Ortega, A., and Tong, X. Tectonic and Anthropogenic Deformation at the Cerro Prieto Geothermal Step-Over Revealed by Sentinel-1A InSAR. *IEEE Transactions on Geoscience and Remote Sensing*, 55(9): 5284–5292, 2017. doi: 10.1109/TGRS.2017.2704593.

Yamanaka, T. and Adachi, I. Hot springs reflect the flooding of slab-derived water as a trigger of earthquakes. *Communications Earth & Environment*, 5(1):459, 2024. doi: 10.1038/s43247-024-01606-1.

Yan, X., Shi, Z., Zhou, P., Zhang, H., and Wang, G. Modeling earthquake-induced spring discharge and temperature changes in a fault zone hydrothermal system. *Journal of Geophysical Research: Solid Earth*, 125(7):e2020JB019344, 2020. doi: 10.1029/2020JB019344.

Yunjun, Z., Fattahi, H., Pi, X., Rosen, P., Simons, M., Agram, P., and Aoki, Y. Range geolocation accuracy of C-/L-band SAR and its implications for operational stack coregistration. *IEEE Transactions on Geoscience and Remote Sensing*, 60:1–19, 2022. doi: 10.1109/TGRS.2022.3168509.